Mechanism and Machine Theory 220 (2026) 106365

Contents lists available at ScienceDirect

Mechanism and Machine Theory

journal homepage: www.elsevier.com/locate/mechmt

Research paper

Integrating the elastic surroundings into multibody simulation of rolling bearings

Tobias Baumann [a,*], Bodo Hahn [b], Stephan Tremmel [a]

[a] Engineering Design and CAD, University of Bayreuth, Universitätsstraße 30, 95447 Bayreuth, Germany
[b] Schaeffler Technologies AG & Co. KG, Industriestraße 1-3, 91074 Herzogenaurach, Germany

ARTICLE INFO

Keywords:
Rolling bearing
Elastic multibody simulation
Dynamic simulation
Finite element analysis
Model reduction
Bearing vibrations

ABSTRACT

Rolling bearings provide secure guidance and load transmission only with sufficient support from the surrounding components (housing, gear body, shaft). In some cases, such as planetary gear bearings or large-size bearings, the stiffness of the bearing surroundings can affect the internal bearing dynamics. Therefore, this article presents a new, computationally efficient method for integrating elastic surroundings, including the rings, into multibody simulation of rolling bearings. Elastic modeling is based on a component mode synthesis method and the floating frame of reference formulation. For the contact calculation between rolling element and ring, a slice model is extended to deformed ring surfaces. The method is applied to spherical roller bearings. Minor mean errors of <4% in the load distribution verify the implemented contact search and force calculation. Additional evaluations of the rolling element speed confirm the correct kinematics of the rolling elements. A plummer block housing demonstrates that the method can account for inhomogeneous stiffness distributions and is not restricted to simple, symmetrical surroundings. Furthermore, it was found that outer ring deformations can lead to increased bearing vibrations.

1. Introduction

Rolling bearings provide secure guidance and load transmission only with sufficient support from the surrounding components (e.g., housing, gear body, or shaft), which is why these components are often designed to be as stiff as possible [1]. However, in some cases, such as planetary gear bearings, large-size rolling bearings, or lightweight design (e.g., hollow shafts), this requirement cannot be met. Planetary gear bearings are supported only by the planet carrier and the meshing of the planet gear with the ring gear and sun gear [2]. For large-size rolling bearings, such as the main bearing in wind turbines, the design of stiff bearing surroundings becomes challenging as the bearing size increases due to space restrictions [1,3]. Therefore, Torsvik et al. [4] and Kock et al. [5] recommend that, during the development and analysis of main bearings, the surrounding components should always be modeled as elastic bodies, since their stiffness has a high impact on the behavior of the main bearing. Lightweight design generally results in more compliant bearing surroundings [1,2]. In many aircraft and aerospace applications, for example, where shafts are hollow or both rings and housings are thin-walled, a significant radial deformation of the bearing may occur [2,6]. Since the stiffness of the bearing surroundings can affect the internal bearing behavior in the described applications, this work aims to integrate bearing surroundings, including the bearing rings, as an elastic body into the multibody simulation of rolling bearings. Due to the motion of the rolling

* Corresponding author.
E-mail addresses: tobias.baumann@uni-bayreuth.de (T. Baumann), hahnbdo@schaeffler.com (B. Hahn), stephan.tremmel@uni-bayreuth.de (S. Tremmel).

https://doi.org/10.1016/j.mechmachtheory.2026.106365
Received 12 December 2025; Received in revised form 13 January 2026; Accepted 13 January 2026
Available online 22 January 2026

elements, rolling bearings are subjected to highly dynamic internal loads, even under static external loads. If additional external dynamic loads occur, such as shocks, vibrations, or speed changes, a quasi-static design is no longer sufficient. Therefore, transient processes in rolling bearings, such as the kinematics and kinetics of the bearing components, can only be analyzed in detail using dynamic simulations, such as multibody simulations [7].

In most studies of bearing dynamics, the components of the bearing are modeled as rigid bodies [8]. These include various planar models, such as ball bearings [9,10], cylindrical roller bearings [11,12], planetary gear systems [13,14], and rolling bearings with defects [12,15,16]. One of the first dynamic simulation programs for rolling bearings as a six-degrees-of-freedom system was ADORE [17,18], based on the work of Gupta [19,20]. These dynamic bearing models were used in various applications, including bearing life prediction [21], vibration response [22], and high-speed ball bearings with thermo-elastohydrodynamic lubrication [23]. Based on the works of Teutsch [24,25], Aul [26], and Kiekbusch [3], the multibody simulation program LaMBDA is being developed at the Chair of Machine Elements, Gears, and Tribology (RPTU University Kaiserslautern-Landau, Germany). Unlike ADORE, LaMBDA is not a standalone program. Instead, it uses SIMPACK and its user subroutines to model deep groove ball bearings, cylindrical roller bearings, and tapered roller bearings [27,28]. The rolling bearing manufacturer NTN pursues a similar approach based on ADAMS [29,30]. Other rolling bearing manufacturers use their own simulation programs, including BEAST [31–35] from SKF, BRAIN [36,37] from NSK, CAGEDYN [38–41] from Timken, and Caba3D [7,42–45] from Schaeffler. As these programs are proprietary know-how, little information is available on their functional scope and calculation methodology. In addition to the mentioned programs, further dynamic models of cylindrical roller bearings [46–48], tapered roller bearings [47], spherical roller bearings [49], angular contact ball bearings [50,51], four point contact bearings [52], and deep groove ball bearings [53–56] exist, in which the bearing components are rigid bodies with mostly six degrees of freedom.

Cages are generally more flexible than rolling elements and rings due to their structural properties. This has led to the development of different elastic cage models. One simplified approach are lumped mass models in which the cage is divided into rigid segments that are flexibly connected [57–59]. This strategy is not suitable for elastic bearing rings, as discontinuities in the contact between rolling element and ring would occur at the interface between two adjacent segments [60]. Another semi-flexible approach involves coupling rigid cage pocket surfaces with flexible cage bars [42,61–63]. This modeling cannot be applied to bearing rings, since the raceways and ribs of the bearing rings rotate through 360° and would therefore remain rigid. A third approach, where the rolling elements interact directly with the finite element mesh of the cage, provides a fully elastic cage model [30,42,64]. The finite element mesh of the surroundings would need to be very fine to ensure that the errors in the contact between rolling element and ring caused by the discretization of the rings are sufficiently small. Due to the high number of degrees of freedom, this solution is computationally impractical.

In most of the dynamic bearing models reviewed so far, global structural deformations of the bearing surroundings are neglected. One simplified approach is to include the effective bearing stiffness in the multibody system. However, this method does not allow for analysis of the internal bearing dynamics. For example, LaCava et al. [65] and Jiang et al. [66] used this strategy to determine the load distribution between planetary gear bearings of a wind turbine drivetrain. Tan et al. [67] incorporated the effective bearing stiffness to investigate the vibration modes of a wind turbine drivetrain. Xu et al. [68] analyzed the vibrations of a flexible rotor system. Another simplified approach is to couple rigid bearing models with an elastic model of their surroundings. Since the inner and outer rings can only perform rigid body motions, the contact surfaces of the rings remain undeformed. Brouwer et al. [69] integrated an elastic shaft and Cao et al. [70] multiple elastic housings as 3D finite element models into the rigid bearing model of Saheta [56]. Shafiee et al. [71] incorporated both an elastic shaft and an elastic housing into a bearing system using the component mode synthesis method [72] in ADAMS. Li et al. [73] and Tian et al. [74] extended Gupta's angular contact ball bearing model [17] by an elastic shaft. Li et al. modeled the elastic shaft with Timoshenko beam elements, and Tian et al. with 3D finite elements.

To investigate the influence of elastic bearing surroundings on the dynamic behavior of bearings in detail, it is necessary to consider the elastic deformations of the bearing rings and their contact surfaces. Various dynamic finite element models exist, most of which are two-dimensional due to the high number of degrees of freedom [75,76]. In bearing models as multibody systems, different approaches are pursued. LaMBDA approximates the deformation of the outer raceway as a function of the load direction and the position of the rolling elements [26,27]. These deformations are precomputed for multiple operating states using static finite element analyses and then linearly interpolated during the multibody simulation for the current operating state. Wagner et al. [77], Leupold et al. [78], and Kiekbusch [3] modeled the rings in the multibody system as finite element models, which are reduced using the Craig-Bampton method [72]. However, they considered the elastic deformations differently. Wagner et al. [77] interpolated the ring deformation at the positions of the balls from the elastic displacements of the adjacent retained nodes using the shape functions of the finite elements. Leupold et al. [78] coupled each ball with non-linear springs to the two closest retained nodes at each time step. Kiekbusch [3] reconstructed the deformed raceway with splines from the displaced positions of the retained nodes and calculated the contacts between the rolling elements and the splines, but without verification. A disadvantage of this procedure is the additional fitting of the splines for the contact calculation at each time step. Fiszer et al. [79] also reconstructed the deformed raceway from a reduced finite element model with splines, but in a different way than Kiekbusch [3]. They fit the eigenmode shapes using B-splines and superimposed the control points of the B-splines and the reduced elastic coordinates to the deformed raceway. Another common approach is to express the structural deformations of the rings by a Fourier series. Cavallaro et al. [6] presented a planar quasi-dynamic model that incorporates radial deformations of the rings by a Fourier series. As the rings and the housing-shaft assembly are treated as simple hollow shafts, the Fourier coefficients are calculated analytically. This approach was also adopted by Defaye et al. [80], Leblanc et al. [81], and Liu et al. [82]. However, Cavallaro et al. [6] highlighted that this model is only suitable for axisymmetric structures and suggested obtaining the Fourier coefficients from finite element analyses to achieve a more accurate solution. The latter approach was taken by Dahiwal et al. [83]. They determined the Fourier coefficients using a fast Fourier transform for the raceway deformations of a

cylindrical roller bearing. So far, the raceway deformations are prespecified by calculating the Fourier coefficients a priori, so that the deformations remain unchanged during the dynamic simulation. Wensing [84] introduced a new component mode synthesis method for describing the radial and axial deformations of the outer raceway of deep groove ball bearings using a Fourier series, where the Fourier coefficients serve as the elastic degrees of freedom. Nakhimovski [32] extended the method of Wensing to radial, tangential, and axial deformations. According to [32], this method is employed in BEAST, however, no elastic bearing models have been presented and verified so far. Similar Fourier series-based approaches were applied by Kerst et al. [85] and Raabe [86] in their quasi-static bearing models.

To sum up, in many applications, the internal behavior of rolling bearings depends on the stiffness of the surrounding components (e.g., housing, gear body, or shaft). Despite numerous previous studies, 3D dynamic bearing models with deformable bearing surroundings, including the bearing rings, and the verification of those models, remain an open research topic. Therefore, the main aims of this paper are as follows: (1) Development of a new and reliable method for integrating bearing surroundings as an elastic body into multibody simulation of rolling bearings at low computational cost. (2) Verification of the proposed method.

First, the method is developed in Section 2. The elastic modeling is based on the finite element analysis, the component mode synthesis method of Wensing [84] and Nakhimovski [32], and the floating frame of reference formulation [87]. Linear elastic material behavior and geometric linearity, i.e., small deformations, are assumed. For the contact calculation between rolling element and ring, a slice model is used, as generally prescribed in ISO 16281 [88] for roller bearings. The contact calculation is extended to deformed ring contact surfaces by superimposing the global constraint modes of the component mode set onto the undeformed contact surfaces. The contributions of the global constraint modes are evaluated at each time step during the multibody simulation. As an example, the method is applied to several spherical roller bearing models. The results are verified in Section 3 against (1) an existing analytical solution by Harris and Kotzalas [2], (2) a finite element analysis solution, and (3) the results of the widely used quasi-static bearing calculation program Bearinx [1,89]. To further investigate the effects of elastic surroundings, vibrations of the inner ring are analyzed in Section 4.

2. Method for integrating elastic bearing surroundings into multibody simulation of rolling bearings

The method is described in detail in Sections 2.1 to 2.4. A spherical roller bearing is used as an example, but the method can also be applied to other types of rolling bearings. The implementation of the developed method is outlined in Section 2.5. Section 2.6 summarizes the spherical roller bearing models investigated.

2.1. Finite element model reduction

The bearing surroundings is first represented as a finite element model with N_{FE} degrees of freedom. As the number of degrees of freedom is usually too large to integrate the finite element model directly into multibody simulation in a computationally efficient manner, it is reduced to $n_{\mathrm{FE}} \ll N_{\mathrm{FE}}$ degrees of freedom while retaining its essential properties. Using the component mode synthesis method developed by Wensing [84] and Nakhimovski [32], the elastic coordinates $\boldsymbol{q}_{\mathrm{e}} \in \mathbb{R}^{N_{\mathrm{FE}}}$ of the non-reduced finite element model are approximated as

$$\boldsymbol{q}_{\mathrm{e}} \approx \boldsymbol{V}_{\mathrm{gc}} \overline{\boldsymbol{q}}_{\mathrm{e}}, \tag{1}$$

where $\boldsymbol{V}_{\mathrm{gc}} \in \mathbb{R}^{N_{\mathrm{FE}} \times n_{\mathrm{FE}}}$ is the coordinate transformation matrix and $\overline{\boldsymbol{q}}_{\mathrm{e}} \in \mathbb{R}^{n_{\mathrm{FE}}}$ are the reduced elastic coordinates. After reducing the finite element model, the elastic displacements u_k of the raceway are expressed in cylindrical coordinates (x, r, φ) as

$$u_k(x,r,\varphi) = \sum_{n=0}^{N_k}\sum_{m=0}^{M_k}\sum_{l=0}^{L_k} a_{k,n,m,l}\cos(n\varphi) T_m\left(\frac{x}{\overline{X}}\right) T_l\left(\frac{r}{\overline{R}}\right) + \sum_{n=1}^{N_k}\sum_{m=0}^{M_k}\sum_{l=0}^{L_k} b_{k,n,m,l}\sin(n\varphi) T_m\left(\frac{x}{\overline{X}}\right) T_l\left(\frac{r}{\overline{R}}\right), \tag{2}$$

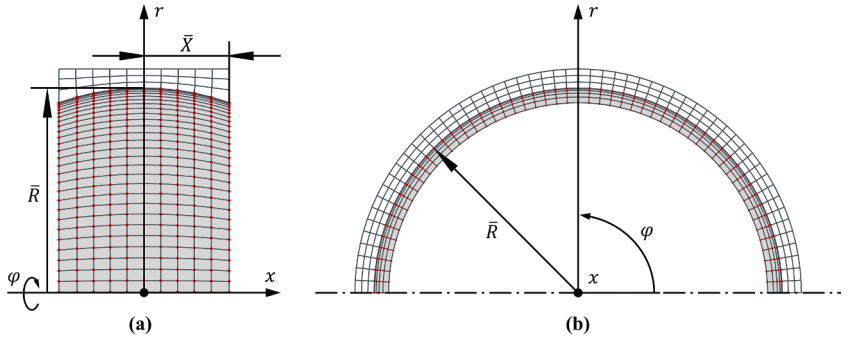

Fig. 1. Schematic finite element model of an outer ring for the definition of the cylinder coordinates (x, r, φ), and the parameters $\overline{X}$ and $\overline{R}$ (see Eq. (2)): (a) section at the x-r-plane and (b) section at $x = 0$.

as shown in Fig. 1. The index k indicates the axial, radial, and tangential directions ($k \in \{x,r,t\}$). For the position dependence, Fourier polynomials are used in the circumferential direction, while Chebyshev polynomials of the first kind, T_m and T_l, are applied in the axial and radial directions. The parameters N_k, M_k, and L_k control the degrees of the polynomials. The arguments of T_m and T_l are scaled with half of the raceway width $\overline{X}$ and the radius $\overline{R}$ of the raceway to $[-1,1]$.

The Chebyshev polynomials of the first kind can be written using trigonometric functions as

$$T_j(\tilde{x}) = \cos(j\arccos(\tilde{x})), |\tilde{x}| \leq 1. \tag{3}$$

The plots of the first five Chebyshev polynomials of the first kind are shown in Fig. 2.

Since Wensing [84] and Nakhimovski [32] do not provide detailed information on the generation of the coordinate transformation matrix $\boldsymbol{V}_{\mathrm{gc}}$, which means that the elastic displacements of the raceway are described by Eq. (2), the procedure followed in this work is explained below. First, the coordinate transformation matrix $\boldsymbol{V}_{\mathrm{c}} \in \mathbb{R}^{N_{\mathrm{FE}} \times N_{\mathrm{b}}}$ according to Guyan [90] is calculated as

$$\boldsymbol{V}_{\mathrm{c}} = \begin{bmatrix} -\boldsymbol{K}_{\mathrm{ii}}^{-1}\boldsymbol{K}_{\mathrm{ib}} \\ \boldsymbol{I}_{\mathrm{bb}} \end{bmatrix}, \tag{4}$$

where $\boldsymbol{I}_{\mathrm{bb}} \in \mathbb{R}^{N_{\mathrm{b}} \times N_{\mathrm{b}}}$ denotes an identity matrix and $\boldsymbol{K}_{\mathrm{ii}} \in \mathbb{R}^{N_{\mathrm{i}} \times N_{\mathrm{i}}}$ and $\boldsymbol{K}_{\mathrm{ib}} \in \mathbb{R}^{N_{\mathrm{i}} \times N_{\mathrm{b}}}$ are submatrices of the stiffness matrix $\boldsymbol{K}_{\mathrm{e}} \in \mathbb{R}^{N_{\mathrm{FE}} \times N_{\mathrm{FE}}}$. The N_{FE} degrees of freedom of the non-reduced model are divided into N_{i} internal and N_{b} boundary degrees of freedom. For the spherical roller bearing, the degrees of freedom of the finite element nodes on the raceway are selected as boundary degrees of freedom. The number of columns of $\boldsymbol{V}_{\mathrm{c}}$ is therefore proportional to the number of raceway nodes.

Each column of $\boldsymbol{V}_{\mathrm{c}}$ corresponds to the static displacement field of the model when a unit displacement is applied to one raceway node, while the remaining degrees of freedom of the raceway nodes are fixed. The columns of $\boldsymbol{V}_{\mathrm{c}}$, also referred to as constraint modes, are modified by

$$\boldsymbol{V}_{\mathrm{gc}} = \boldsymbol{V}_{\mathrm{c}}\boldsymbol{T} \tag{5}$$

to the global constraint modes $\boldsymbol{V}_{\mathrm{gc}} \in \mathbb{R}^{N_{\mathrm{FE}} \times n_{\mathrm{FE}}}$. The columns of $\boldsymbol{T} \in \mathbb{R}^{N_{\mathrm{b}} \times n_{\mathrm{FE}}}$ are the displacement fields of the raceway nodes, when in Eq. (2) one Fourier coefficient equals one, while the remaining Fourier coefficients are set to zero. Thus, $\boldsymbol{T}$ is composed of

$$\boldsymbol{T} = [\,\boldsymbol{T}_x \quad \boldsymbol{T}_r \quad \boldsymbol{T}_t\,] \tag{6}$$

with the submatrices

$$\boldsymbol{T}_k = \left[\boldsymbol{u}_{a_{0,0,0}} \quad \cdots \quad \boldsymbol{u}_{a_{N_k,M_k,L_k}} \quad \cdots \quad \boldsymbol{u}_{b_{1,0,0}} \quad \cdots \quad \boldsymbol{u}_{b_{N_k,M_k,L_k}}\right]_k \tag{7}$$

and $k \in \{x,r,t\}$. The number of columns of $\boldsymbol{T}_k$ is $(2N_k+1)(M_k+1)(L_k+1)$.

The columns of $\boldsymbol{V}_{\mathrm{gc}}$ are the resulting displacement fields of the entire finite element model due to the predefined displacement fields on the raceway in $\boldsymbol{T}$. The space of elastic displacements of the raceway is therefore defined by $\boldsymbol{V}_{\mathrm{gc}}$. After reducing the finite element model with $\boldsymbol{V}_{\mathrm{gc}}$, the reduced elastic coordinates $\overline{\boldsymbol{q}}_{\mathrm{e}}$ from Eq. (1) are composed of

$$\overline{\boldsymbol{q}}_{\mathrm{e}} = [\,\boldsymbol{a}_x \quad \boldsymbol{b}_x \quad \boldsymbol{a}_r \quad \boldsymbol{b}_r \quad \boldsymbol{a}_t \quad \boldsymbol{b}_t\,]^{\mathrm{T}}, \tag{8}$$

where $\boldsymbol{a}_k \in \mathbb{R}^{(N_k+1)(M_k+1)(L_k+1)}$ and $\boldsymbol{b}_k \in \mathbb{R}^{N_k(M_k+1)(L_k+1)}$ with $k \in \{x,r,t\}$ denote the Fourier coefficients of Eq. (2).

Eqs. (2) and (8) show the advantages of the described reduction method over approaches such as Guyan [90] or Craig-Bampton [72] for elastic multibody simulations of rolling bearings. The elastic displacements of the raceway are described by smooth global functions rather than by discrete finite element nodes, allowing the displacements to be evaluated at any point on the raceway. In

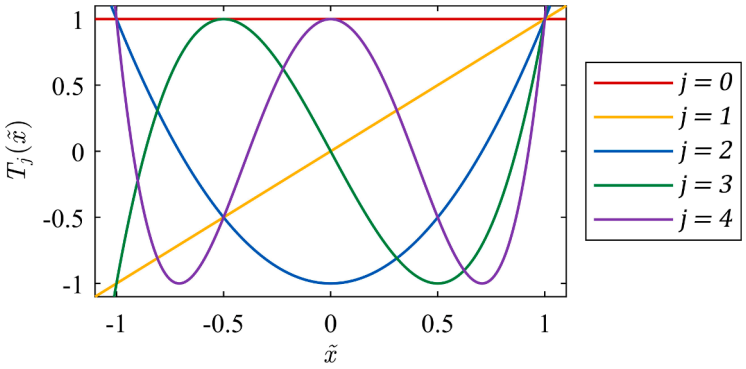

Fig. 2. Plot of the first five Chebyshev polynomials of the first kind.

addition, the n_{FE} degrees of freedom of the reduced finite element model are not proportional to the number of raceway nodes but depend on N_k, M_k, and L_k.

For the integration of the reduced finite element model into the rolling bearing multibody system, the mass matrix $\boldsymbol{M}_{\mathrm{e}} \in \mathbb{R}^{N_{\mathrm{FE}} \times N_{\mathrm{FE}}}$, damping matrix $\boldsymbol{D}_{\mathrm{e}} \in \mathbb{R}^{N_{\mathrm{FE}} \times N_{\mathrm{FE}}}$, and stiffness matrix $\boldsymbol{K}_{\mathrm{e}} \in \mathbb{R}^{N_{\mathrm{FE}} \times N_{\mathrm{FE}}}$ are reduced using the coordinate transformation matrix $\boldsymbol{V}_{\mathrm{gc}}$:

$$\overline{\boldsymbol{M}}_{\mathrm{e}} = \boldsymbol{V}_{\mathrm{gc}}^{\mathrm{T}} \boldsymbol{M}_{\mathrm{e}} \boldsymbol{V}_{\mathrm{gc}}, \quad \overline{\boldsymbol{D}}_{\mathrm{e}} = \boldsymbol{V}_{\mathrm{gc}}^{\mathrm{T}} \boldsymbol{D}_{\mathrm{e}} \boldsymbol{V}_{\mathrm{gc}} \text{and} \quad \overline{\boldsymbol{K}}_{\mathrm{e}} = \boldsymbol{V}_{\mathrm{gc}}^{\mathrm{T}} \boldsymbol{K}_{\mathrm{e}} \boldsymbol{V}_{\mathrm{gc}}. \tag{9}$$

The matrices of the reduced model are denoted by $\overline{\boldsymbol{M}}_{\mathrm{e}} \in \mathbb{R}^{n_{\mathrm{FE}} \times n_{\mathrm{FE}}}$, $\overline{\boldsymbol{D}}_{\mathrm{e}} \in \mathbb{R}^{n_{\mathrm{FE}} \times n_{\mathrm{FE}}}$, and $\overline{\boldsymbol{K}}_{\mathrm{e}} \in \mathbb{R}^{n_{\mathrm{FE}} \times n_{\mathrm{FE}}}$.

2.2. Elastic multibody dynamics

The equations of motion of the rigid bearing components (inner ring, cage, and rolling elements) are presented in [43]. To integrate the reduced finite element models of bearing surroundings, the floating frame of reference formulation [87,91] is employed. As this formulation is a well-established approach for modeling elastic multibody systems, only the relevant aspects and their modifications for elastic bearing surroundings are provided below. The description of kinematics and equations of motion of an elastic body used in this work are derived in [91].

According to the floating frame of reference formulation [87,91], the motion of an elastic body within the inertial frame is superimposed by large, nonlinear rigid body motions of a body-related reference frame $\mathrm{K_R}$ and small, linear-elastic displacements ${}^{\mathrm{R}}\boldsymbol{u}$ with respect to this frame, which is indicated by the left superscript R. The reference frame $\mathrm{K_R}$ can be defined in different ways, in this work, the Buckens frame [87,91] is selected. To ensure that the coordinate transformation matrix $\boldsymbol{V}_{\mathrm{gc}}$ satisfies the boundary conditions imposed by the Buckens frame, $\boldsymbol{V}_{\mathrm{gc}}$ is modified as described in [91]. According to the Rayleigh-Ritz method [87,91], the elastic displacements ${}^{\mathrm{R}}\boldsymbol{u}$ of a point ${}^{\mathrm{R}}\boldsymbol{c}$ are approximated at time t as

$${}^{\mathrm{R}}\boldsymbol{u}\left(t, {}^{\mathrm{R}}\boldsymbol{c}\right) = \boldsymbol{\Phi}\left({}^{\mathrm{R}}\boldsymbol{c}\right)\boldsymbol{q}_{\mathrm{e}}(t) \tag{10}$$

with the global shape matrix $\boldsymbol{\Phi}$ and the time-dependent elastic coordinates $\boldsymbol{q}_{\mathrm{e}}(t)$. Since Eq. (2) is used as global shape functions, the elastic displacements of any point on the raceway can be calculated as

$${}^{\mathrm{R}}\boldsymbol{u}\left(t, {}^{\mathrm{R}}\boldsymbol{c}\right) = \mathbf{V}_{\mathrm{gc}}\left({}^{\mathrm{R}}\boldsymbol{c}\right)\overline{\boldsymbol{q}}_{\mathrm{e}}(t) \tag{11}$$

from the time-dependent reduced elastic coordinates $\overline{\boldsymbol{q}}_{\mathrm{e}}(t)$. The columns of $\mathbf{V}_{\mathrm{gc}}\left({}^{\mathrm{R}}\boldsymbol{c}\right) \in \mathbb{R}^{3 \times n_{\mathrm{FE}}}$ are the global constraint modes evaluated at point ${}^{\mathrm{R}}\boldsymbol{c}$.

2.3. Raceway geometry

The undeformed outer surfaces of the bearing rings, including the internal contact surfaces, are created by rotating a two-dimensional profile around the bearing axis. For example, the raceway profile of the outer ring of a spherical roller bearing is a circular arc segment, as shown in Fig. 3. The raceway profile $\boldsymbol{p}(u)$ is described using the parameter u as

$$\boldsymbol{p}(u) = \begin{bmatrix} p_x(u) \\ p_y(u) \end{bmatrix} = \begin{bmatrix} R\cos(2\pi u) \\ R\sin(2\pi u) \end{bmatrix} \tag{12}$$

with $u \in [u_{\min}, u_{\max}]$. The boundaries of the raceway profile are at $\boldsymbol{p}(u_{\min})$ and $\boldsymbol{p}(u_{\max})$.

Rotating the raceway profile $\boldsymbol{p}(u)$ around the bearing axis using a second parameter v results in the undeformed three-dimensional raceway surface

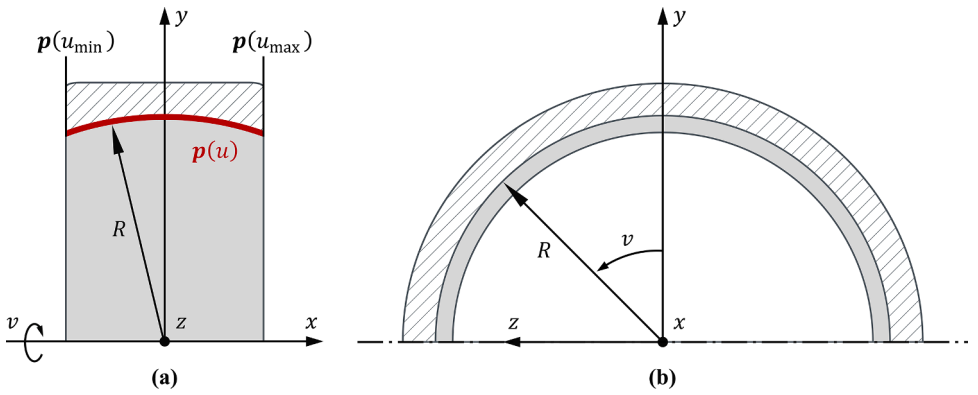

Fig. 3. Raceway of the outer ring of a spherical roller bearing: (a) two-dimensional profile $\boldsymbol{p}(u)$ and (b) side view with section at the y-z-plane.

$$\boldsymbol{s}_0(u,v) = \begin{bmatrix} s_{0,x}(u) \\ s_{0,y}(u,v) \\ s_{0,z}(u,v) \end{bmatrix} = \begin{bmatrix} p_x(u) \\ p_y(u)\cos(2\pi v) \\ p_y(u)\sin(2\pi v) \end{bmatrix} \tag{13}$$

with $u \in [u_{\min}, u_{\max}]$ and $v \in [0,1]$. Eq. (13) describes the spherical raceway of the outer ring of a spherical roller bearing.

The elastic displacements of the raceway are expressed by Eq. (2). To describe the elastic displacements u_k mathematically consistent with the undeformed raceway surface $\boldsymbol{s}_0$, Eq. (2) must be transformed into the parameter form of Eq. (13):

$$u_k(u,v,t) = \sum_{n=0}^{N_k}\sum_{m=0}^{M_k}\sum_{l=0}^{L_k} a_{k,n,m,l}(t)\cos(n2\pi v)T_m\left(\frac{p_x(u)}{\overline{X}}\right)T_l\left(\frac{p_y(u)}{\overline{R}}\right) + \sum_{n=1}^{N_k}\sum_{m=0}^{M_k}\sum_{l=0}^{L_k} b_{k,n,m,l}(t)\sin(n2\pi v)T_m\left(\frac{p_x(u)}{\overline{X}}\right)T_l\left(\frac{p_y(u)}{\overline{R}}\right) \tag{14}$$

with $k \in \{x,r,t\}$. The Fourier coefficients $a_{k,n,m,l}(t)$ and $b_{k,n,m,l}(t)$ show the dependence of the reduced elastic coordinates $\overline{\boldsymbol{q}}_e$ on time t (see Eq. (11)).

Finally, the deformed raceway surface $\boldsymbol{s}_1$ is calculated as the sum of the undeformed raceway surface $\boldsymbol{s}_0$ and the time-dependent elastic displacements $\boldsymbol{u}$:

$$\boldsymbol{s}_1(u,v,t) = \boldsymbol{s}_0(u,v) + \boldsymbol{u}(u,v,t) = \begin{bmatrix} s_{0,x} \\ s_{0,y} \\ s_{0,z} \end{bmatrix} + \begin{bmatrix} u_x(u,v,t) \\ u_r(u,v,t)\cos(2\pi v) - u_t(u,v,t)\sin(2\pi v) \\ u_r(u,v,t)\sin(2\pi v) + u_t(u,v,t)\cos(2\pi v) \end{bmatrix}. \tag{15}$$

The elastic displacements are therefore transformed into the Cartesian coordinate system of the raceway surface $\boldsymbol{s}_0$.

2.4. Contact calculation

This section describes the contact calculation between rolling elements and rings, which is extended to deformed raceway surfaces. The rolling elements are rigid bodies. As generally prescribed in ISO 16281 [88] for roller bearings, the slice model of Section 2.4.1 is used. During the contact calculation, each slice is checked for penetration with the deformed raceway surface (see Section 2.4.2). If penetration is detected, the contact forces are calculated (see Section 2.4.3).

2.4.1. Slice model

To account for influences such as the rolling element profile, as well as tilting and skewing of the rolling elements, a slice model is commonly used in bearing calculations, for instance in [17,24,26,29,30,46,47,88,92]. In this work, the slice model of Vesselinov [43] is employed, in which the geometry of the rolling elements is discretized in detail. Interactions between the slices are neglected as a trade-off between simulation accuracy and computational cost, since the precise pressure distribution along the rolling element axis is not the focus of this paper [24,92].

Each rolling element is divided into n_s slices as shown in Fig. 4. Each slice contributes to the rolling element stiffness based on its size. For the contact search, each slice is described by a circle, which is the intersection curve of the rolling element surface and the slice plane. The slice radii r_i can vary along the length of the rolling element. In addition, the surface normals $\boldsymbol{n}_i$ of the slices point in the direction of the actual normals of the rolling element surface.

2.4.2. Contact search

Due to external loads on the rolling bearing, local contact deflections occur between the rolling elements and the raceway, allowing the contact partners to approach each other and form a contact surface. A rolling element is in contact with the raceway when slices

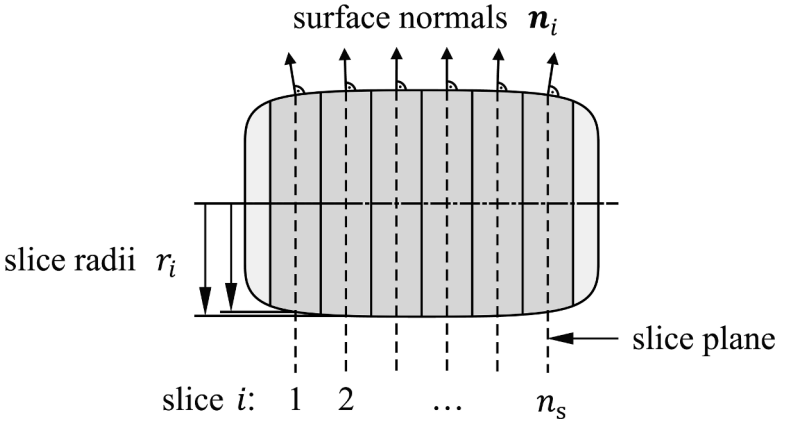

Fig. 4. Slice model of the rolling element.

penetrate the raceway. These penetrations correspond to the local contact deflections, while the intersection points of the slices with the raceway describe the contour of the contact surface.

Fig. 5 shows a slice in contact with the raceway. The results of the contact search are the contact point $\boldsymbol{x}_c$, the contact normal $\boldsymbol{n}_c$, the penetration p of the two contact partners, and the contact width w. These geometric contact variables are determined for each slice during the contact search. In the following, the variables of the slice are indicated with the exponent (0), while the exponent (1) denotes the variables of the deformed raceway surface.

The contact point $\boldsymbol{x}_c$ is located between the penetration points $\boldsymbol{x}_p^{(0)}$ and $\boldsymbol{x}_p^{(1)}$. The latter is the point on the deformed raceway surface $\boldsymbol{s}_1$ that is closest to the center point $\boldsymbol{x}_c^{(0)}$ of the slice and lies within the slice plane. To find the point $\boldsymbol{x}_p^{(1)}$, the restricted optimization problem

$$\begin{aligned} &\min\ d(u,v)^2 = \min \| \boldsymbol{x}_c^{(0)} - \boldsymbol{s}_1(u,v) \|_2^2 \\ &\quad s.t.\ h(u,v) = 0 \end{aligned} \tag{16}$$

is solved numerically using the Lagrange-Newton approach. Instead of minimizing the Euclidean distance $d(u,v)$ between $\boldsymbol{x}_c^{(0)}$ and a point on the surface $\boldsymbol{s}_1$, the squared Euclidean distance is minimized. The constraint

$h(u,v) = 0$ ensures that $\boldsymbol{x}_p^{(1)}$ lies within the slice plane and is formulated as

$$h(u,v) = \left(\boldsymbol{n}^{(0)}\right)^{\mathrm{T}} \left(\boldsymbol{s}_1(u,v) - \boldsymbol{x}_c^{(0)}\right) = 0 \tag{17}$$

with the normal vector $\boldsymbol{n}^{(0)}$ of the plane. The solution (u_p, v_p) is only valid if $u_p \in [u_{\min}, u_{\max}]$, otherwise the point $\boldsymbol{x}_p^{(1)} = \boldsymbol{s}_1(u_p, v_p)$ is not on the raceway. If the point $\boldsymbol{x}_p^{(1)}$ is valid, the second penetration point $\boldsymbol{x}_p^{(0)}$is calculated as

$$\boldsymbol{x}_p^{(0)} = \boldsymbol{x}_c^{(0)} + r \frac{\boldsymbol{x}_p^{(1)} - \boldsymbol{x}_c^{(0)}}{\| \boldsymbol{x}_p^{(1)} - \boldsymbol{x}_c^{(0)} \|_2}. \tag{18}$$

with the slice radius r. The contact normal $\boldsymbol{n}_c$ is determined from the surface normal $\boldsymbol{n}_p^{(0)}$ at the point $\boldsymbol{x}_p^{(0)}$ and $\boldsymbol{n}_p^{(1)}$ at the point $\boldsymbol{x}_p^{(1)}$. In the general case where $\boldsymbol{n}_p^{(0)}$ and $\boldsymbol{n}_p^{(1)}$ are not collinear and opposite, $\boldsymbol{n}_c$ points in the direction of the angle bisector between $\boldsymbol{n}_p^{(0)}$ and $\boldsymbol{n}_p^{(1)}$ (see Fig. 5(b) and (c)).

The penetration p is the Euclidean distance between the two penetration points $\boldsymbol{x}_p^{(0)}$ and $\boldsymbol{x}_p^{(1)}$. The contact width w is estimated as

$$w = 2\sqrt{2rp} \tag{19}$$

based on the intersection of a circle with a plane. As the penetration p is very small and the radius R of the raceway is significantly larger than the radius r of the slice, Eq. (19) provides a good approximation of the contact width w. Finally, the intersection points $\boldsymbol{x}_{i,1}$ and $\boldsymbol{x}_{i,2}$ are calculated as

$$\boldsymbol{x}_{i,1/2} = \boldsymbol{x}_p^{(1)} \pm \frac{w}{2} \boldsymbol{t}_p^{(1)}, \tag{20}$$

where the vector $\boldsymbol{t}_p^{(1)}$ is the normalized cross product of the normal vector $\boldsymbol{n}^{(0)}$ of the slice plane and the vector from the center point $\boldsymbol{x}_c^{(0)}$ to the penetration point $\boldsymbol{x}_p^{(1)}$.

2.4.3. Contact force calculation

The contact forces are calculated individually for each slice based on the results of the contact search. The resulting contact forces

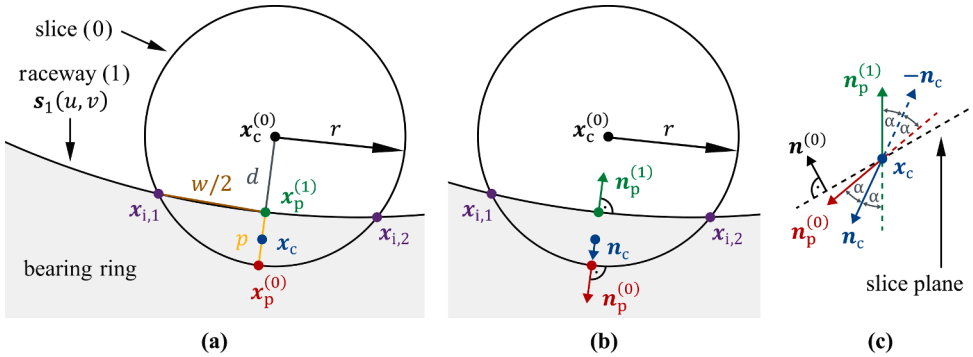

Fig. 5. Contact search. The view is perpendicular to the slice plane in (a) and (b) and rotated by 90° in (c).

include contact normal, damping, and friction force components. As the contact force models used are well-established in rolling bearing dynamics, they are only briefly described. However, all adjustments due to the elastic modeling of bearing surroundings are explained in detail. Furthermore, the use of alternative existing contact force models is also conceivable, but it is beyond the scope of this work.

There are various contact normal force models based on different theoretical or empirical load-deflection relationships. An overview can be found in [24]. In this work, the contact normal force $F_{c,n}$ is calculated for each slice as

$$F_{c,n} = c_1 p^{c_2} \frac{l_s}{l_c} \tag{21}$$

depending on the penetration p of each slice, the constants c_1 and c_2, the slice length l_s, and the contact length l_c. The constants are determined according to Lundberg [93].

The damping force includes material and lubricant damping. The material damping force is calculated according to Sjö [94] as

$$F_{d,m} = -F_{c,n} c_{d1} \arctan\left(\frac{\Delta v_n}{c_{d2}}\right) \frac{2}{\pi} \tag{22}$$

with the relative velocity Δv_n of the contact point in the normal direction and the model parameters c_{d1} and c_{d2}. The lubricant damping force $F_{d,l}$ considers the damping characteristics of the lubricant film. Using TELOS [95], which is a Schaeffler in-house rolling contact simulation program, a parametric equation for $F_{d,l}$ has been derived. The lubricant damping force $F_{d,l}$ is calculated based on the contact normal force $F_{c,n}$, geometric contact results, contact velocities, and lubricant parameters. An overview of various alternative damping models, including the approach developed by Dietl [96], can be found in [3].

The friction force F_r includes components of rolling and sliding friction in solid and lubricated conditions. The lubricant friction is calculated based on the elasto-hydrodynamic lubrication theory. Similar friction force models to those used in this work are presented in [2,28].

The calculation of the damping and friction forces requires velocities at the contact point, which are extended by the deformation velocity of the elastic bearing rings. Similar to Eq. (1), the deformation velocity $\dot{\boldsymbol{q}}_c \in \mathbb{R}^3$ at the contact point is determined by

$$\dot{\boldsymbol{q}}_c = \boldsymbol{V}_{gc}\left(\boldsymbol{x}_p^{(1)}\right)\dot{\bar{\boldsymbol{q}}}_e \tag{23}$$

from the velocities $\dot{\bar{\boldsymbol{q}}}_e \in \mathbb{R}^{n_{FE}}$ of the reduced elastic coordinates with the coordinate transformation matrix $\boldsymbol{V}_{gc}\left(\boldsymbol{x}_p^{(1)}\right) \in \mathbb{R}^{3\times n_{FE}}$. The global constraint modes $\boldsymbol{V}_{gc}$ of Eq. (5) are evaluated at the penetration point $\boldsymbol{x}_p^{(1)}$ rather than at the contact point $\boldsymbol{x}_c$, because Eq. (2) describes only the elastic displacements of the raceway and the contact point $\boldsymbol{x}_c$ is located slightly inside the bearing ring (see Fig. 5 (a)). Since the penetration p is small, Eq. (23) is a good approximation. $\boldsymbol{V}_{gc}\left(\boldsymbol{x}_p^{(1)}\right)$ must be recalculated for each contacting slice and at each time step.

After calculating the contact normal, damping, and friction forces, the components are added to the resulting contact forces for each slice, considering the respective directions of the force components. The resulting contact force $\boldsymbol{h}_c \in \mathbb{R}^3$ is then applied to the reduced elastic coordinates by

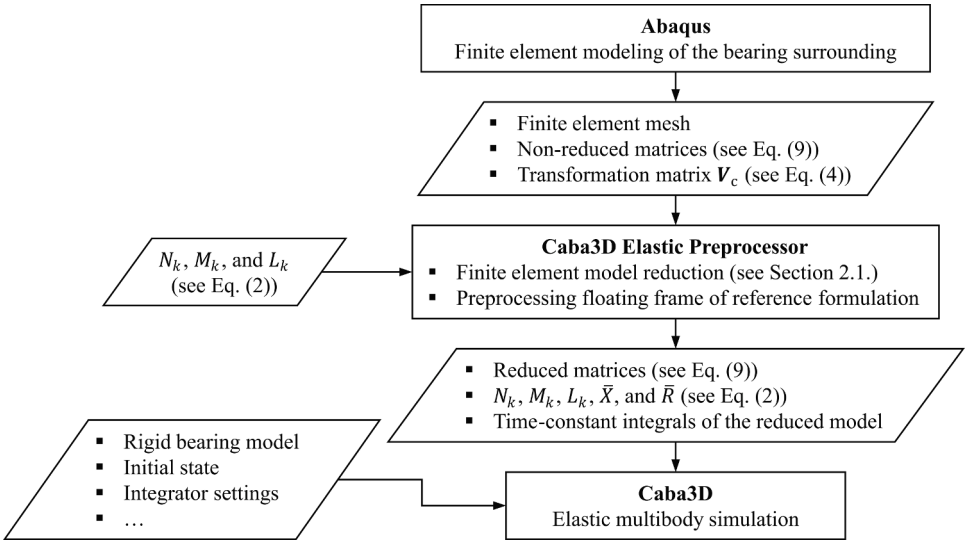

Fig. 6. Flowchart of the modeling process of elastic bearing surroundings in Caba3D.

$$\overline{\boldsymbol{h}}_{\mathrm{c}} = \boldsymbol{V}_{\mathrm{gc}}^{\mathrm{T}}\left(\boldsymbol{x}_{\mathrm{p}}^{(1)}\right)\boldsymbol{h}_{\mathrm{c}}. \tag{24}$$

2.5. Software implementation

The method described in Sections 2.1 to 2.4 was implemented in Caba3D [7,42–45], a Schaeffler in-house multibody simulation software for rolling bearings, which is continuously validated against experiments [97–99] and simulations [42,43,45,91]. It allows the calculation of the dynamics of all rolling bearing components in the time domain. By default, the rolling bearing components are modeled as rigid bodies with six degrees of freedom and the equations of motion presented in [43]. In addition, an elastic cage model with two different contact calculation methods is available [42]. The cage is represented as a finite element model, which is reduced according to the Craig-Bampton method [72] and integrated into the rolling bearing multibody system using the floating frame of reference formulation [87,91]. For contact calculation, either a slice model with rigid cage pockets or a node-to-surface approach can be used, which are described in detail in [42]. As discussed in Section 1, this modeling strategy for elastic cages is not suitable for elastic bearing surroundings, including the bearing rings.

The modeling process of elastic bearing surroundings in Caba3D is outlined in Fig. 6. Finite element modeling is performed in Abaqus/CAE. The Caba3D Elastic Preprocessor [42] generates the reduced mass, damping, and stiffness matrices together with the time-constant integrals of the reduced model according to the floating frame of reference formulation [87,91]. The global constraint modes $\boldsymbol{V}_{\mathrm{gc}}$ required for the finite element model reduction are calculated in the Caba3D Elastic Preprocessor, based on the constraint modes $\boldsymbol{V}_{\mathrm{c}}$ exported from Abaqus/CAE. To this end, the cylindrical coordinate system shown in Fig. 1 is defined automatically, the coordinates of the raceway nodes are imported from the finite element mesh, and the displacement fields of the raceway nodes in $\boldsymbol{T}$ are calculated according to Eq. (2) using the user inputs N_k, M_k, and L_k. To evaluate Eq. (2), the parameters $\overline{X}$ and $\overline{R}$ (see Fig. 1) are automatically determined from the finite element mesh.

The solution algorithm of Caba3D for rolling bearing models with elastic bearing surroundings is illustrated in Fig. 7. During the contact calculation between the rolling elements and an elastic bearing ring, the restricted optimization problem Eq. (16) is solved. Since deformed raceway surfaces are time-dependent according to Eq. (15), Eq. (15) is reevaluated at each time step during the contact calculation. This means that the elastic deformations are not specified in advance but depend on the values of the Fourier coefficients, which are influenced by the dynamic operating conditions (e.g., position of the rolling elements, internal load distribution, etc.). The resulting differential equations of motion are numerically integrated using the Runge–Kutta–Fehlberg method, as implemented in [100]. The time step size Δt is set to 10^{-3} s during the settling phase and to 10^{-6} s for the evaluation.

2.6. Spherical roller bearing models

The developed method for integrating elastic bearing surroundings into multibody simulation of rolling bearings is applied to three different models of the spherical roller bearing 22328-E1-XL:

- Single contact model between rolling element and outer ring (see Section 2.6.1)
- Spherical roller bearing model (see Section 2.6.2)
- Plummer block housing model (see Section 2.6.3)

The properties of the spherical roller bearing 22328-E1-XL, including geometric and performance data, the material properties, and the lubricant, are listed in Table 1. The number of slices per rolling element is $n_{\mathrm{S}} = 100$ for each model. The rolling elements, cage, and

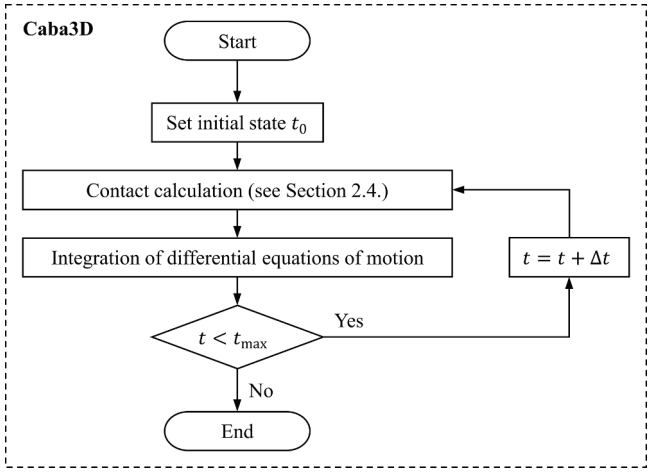

Fig. 7. Flowchart of the solution algorithm of Caba3D.

inner ring are rigid bodies with six degrees of freedom. The outer ring and the plummer block housing are modeled as elastic bodies and, for comparison, as rigid bodies. The elastic bodies are based on the finite element models described in Section 2.6.4. Gravity acts in the y-direction.

2.6.1. Single contact model between rolling element and outer ring

The first model is illustrated in Fig. 8. The external force $F_{\mathrm{RE}} = 35$ kN presses the stationary rolling element into the elastic outer ring, which rotates at a constant speed, causing the outer ring to deform and the rolling element to accelerate. The rigid body degrees of freedom of the outer ring are locked, which means that the outer ring is fixed in its center of gravity. As the rest of the bearing components are not modeled, any complex interactions between them are disregarded. This allows the contact between the rolling element and the raceway to be evaluated independently.

2.6.2. Spherical roller bearing model

The second model of the spherical roller bearing 22328-E1-XL is shown in Fig. 9. An external force F_{IR} is applied to the rigid inner ring and transferred to the elastic outer ring by the rolling elements. The inner ring rotates at a constant speed n_{IR}, and the outer ring is fixed in its center of gravity. The external force F_{IR} and speed n_{IR} are varied according to the operating states in Table 2, which are selected to load the rolling bearing with radial and combined forces in the low, medium, and high-speed ranges. The radial force $F_{\mathrm{r}} = 1,085$ kN corresponds to the basic static load rating $C_{0\mathrm{r}} = 1,630$ kN, considering the static load safety factor $S_0 = 1.5$. The rotational speed $n_{\mathrm{IR}} = 2,420\mathrm{min}^{-1}$ is the limiting rotational speed n_{G} (see Table 1).

2.6.3. Plummer block housing model

The third model of the spherical roller bearing 22328-E1-XL, mounted in the split plummer block housing SNS3136, is shown in Fig. 10. The outer ring and the housing are modeled as one elastic body. The bottom of the housing is fixed. An external force F_{IR} is applied to the inner ring, which rotates at a constant speed $n_{\mathrm{IR}} = 2{,}420\ \mathrm{min}^{-1}$. The properties of the housing, including geometric and performance data as well as its material characteristics, are summarized in Table 3. Due to the inhomogeneous stiffness distribution of the housing, the internal rolling bearing dynamics are expected to depend on the direction α of the radial component of F_{IR}. Thus, the direction α and the external force F_{IR} are varied as listed in Table 4. The radial force of the operating state 1 corresponds to the radial force of the operation state 4 of the spherical roller bearing without housing (see Table 2). The remaining radial forces are adapted according to the ratios of the static housing rupture loads in Table 3.

2.6.4. Finite element models

The finite element models of the outer ring and the plummer block housing for the spherical roller bearing models described in Sections 2.6.1 to 2.6.3 are shown in Fig. 11. The modeling was performed in Abaqus/CAE 2023. The geometry and material properties of the finite element models are consistent with the data in Tables 1 and 3. The outer ring is meshed with 3360 linear hexahedral elements (C3D8) and a total number of 4928 nodes. The plummer block housing is split into an upper and lower half, both of which are meshed with quadratic tetrahedral elements (C3D10). The upper half comprises a total of 19,980 elements and 33,717 nodes, while the lower half has 39,172 elements and 64,121 nodes. The outer ring is mounted in the split plummer block housing. Since no relative motions are assumed between the outer ring and the housing, as well as between the upper and lower halves of the housing, the meshes are tied at the contact surfaces. Regarding the finite element model reduction, both finite element models have 1232 nodes on the raceway, resulting in $N_{\mathrm{b}} = 3696$ boundary degrees of freedom. This is also the number of constraint modes, i.e., the number of columns of $\boldsymbol{V}_{\mathrm{c}}$ (see Eq. (4)). The modification of $\boldsymbol{V}_{\mathrm{c}}$ to $\boldsymbol{V}_{\mathrm{gc}}$ according to Eq. (5) and the required parameters N_k, M_k, and L_k with $k \in \{x, r, t\}$ are investigated in Section 3.

Table 1
Properties of the spherical roller bearing 22328-E1-XL.

Group	Parameter	Symbol	Value	Unit
Geometric data	Bore diameter	d	140	mm
	Outside diameter	D	300	mm
	Width	B	102	mm
	Rows of rolling elements	–	2	–
	Number of rolling elements per row	–	14	–
Performance data	Basic dynamic load rating, radial	C_{r}	1460	kN
	Basic static load rating, radial	$C_{0\mathrm{r}}$	1630	kN
	Limiting rotational speed	n_{G}	2420	min^{-1}
	Static load safety factor[1]	S_0	1.5	–
Material[2] properties of rings and rolling elements	Youngs modulus	E	207,000	$\mathrm{N/mm}^2$
	Poisson's ratio	ν	0.3	–
	Density	ρ	7.81	$\mathrm{kg/dm}^3$
Lubricant	Reference oil	–	FVA100	–

[1] Normal, smooth running, free from vibrations, normal rotational accuracy.
[2] Hardened rolling bearing steel 100Cr6.

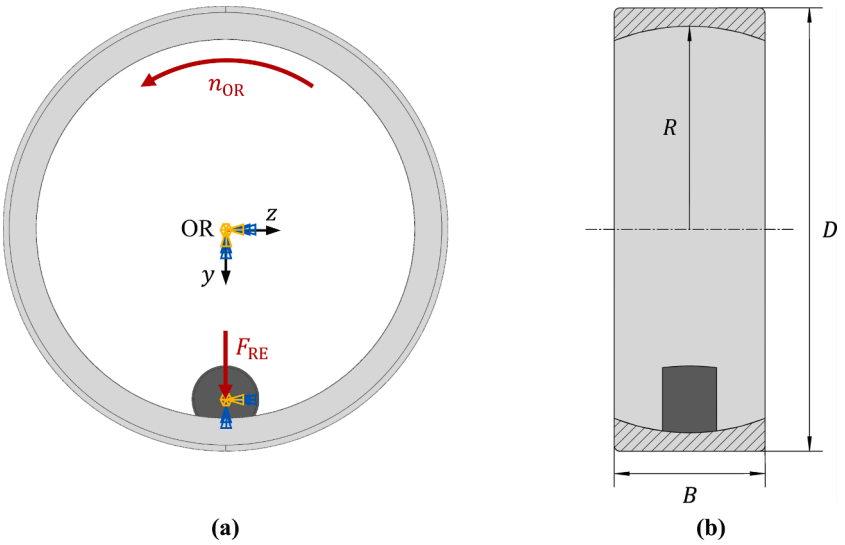

Fig. 8. Single contact model between rolling element and outer ring (OR): (a) boundary conditions and (b) geometric dimensions of the outer ring (see Table 1).

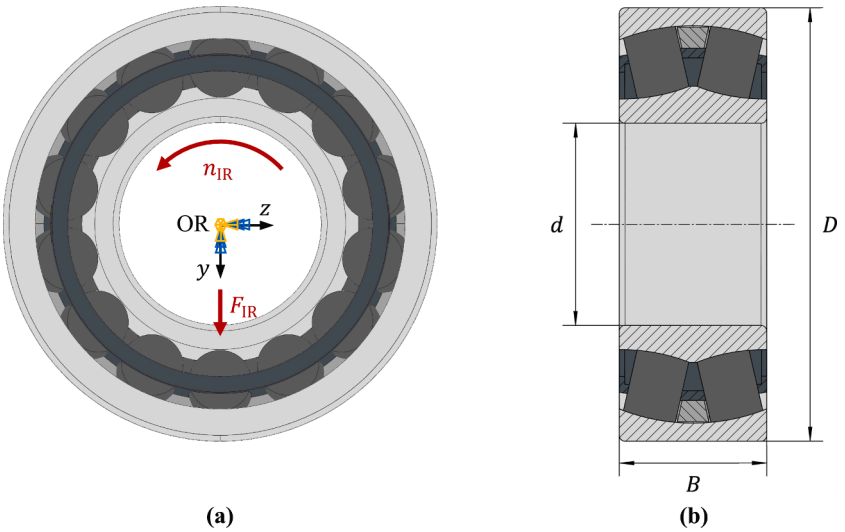

Fig. 9. Spherical roller bearing model: (a) boundary conditions and (b) geometric dimensions (see Table 1).

Table 2
Operating states of the spherical roller bearing 22328-E1-XL.

No.	Radial force F_r in kN	Axial force F_a in kN	Speed n_{1R} in min^{-1}
1	1085	0	0
2	530	0	1210
3	397.5	67	1210
4	430	0	2420
5	265	0	1210

3. Method verification

The spherical rolling bearing models from Section 2.6 were modeled and simulated in Caba3D. To verify the proposed method for integrating elastic bearing surroundings into multibody simulation of rolling bearings, several results are analyzed in Section 3.2 as outlined in Section 3.1. The results and the developed method are discussed in Section 3.3. In general, nine parameters N_k, M_k, and L_k

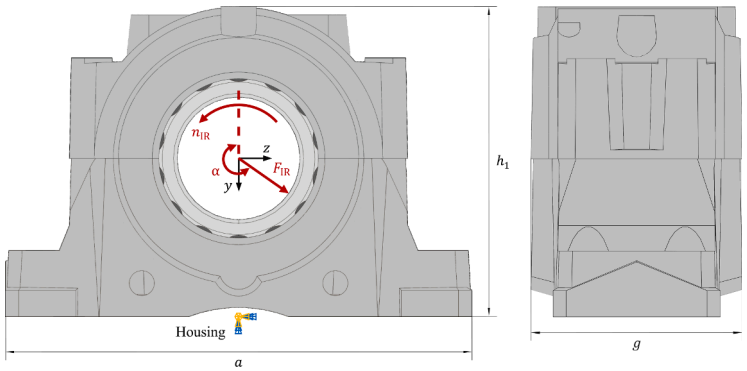

Fig. 10. Pummer block housing model: boundary conditions and geometric dimensions (see Table 3).

Table 3
Properties of the plummer block housing SNS3136.

Group	Parameter	Symbol	Value	Unit
Geometric data	Housing height	h_1	353	mm
	Housing width	G	240	mm
	Length base	a	530	mm
Performance data	Static housing rupture load, radial, 180°	–	4400	kN
	Static housing rupture load, radial, 235°	–	4940	kN
	Static housing rupture load, radial, 270°	–	3300	kN
	Safety factor	S	5	–
Material[1] properties	Youngs modulus	E	169,000	N/mm^2
	Poisson's ratio	ν	0.26	–
	Density	ρ	7.81	kg/dm^3

[1] Spheroidal graphite cast iron EN-GJS-400–15.

Table 4
Operating states of the plummer block housing SNS3136.

No.	Radial force F_r in kN	Axial force F_a in kN	Direction α of F_r in°	Speed n_{1R} in min^{-1}
1	430	0	180	2420
2	322.5	35	180	2420
3	482.75	0	235	2420
4	362	35	235	2420
5	322.5	0	270	2420
6	241.875	35	270	2420

with $k \in \{x, r, t\}$ are required for the finite element reduction. However, since the same values are used in the axial, radial, and tangential directions, the index k is omitted in the following, and only the parameters N, M, and L are specified.

3.1. Simulation based verification process

Several results are evaluated in a multi-stage verification process. First, the radial ring deflection at the position of the rolling element and the rolling element speed are analyzed in the single contact model (see Section 3.2.1). The rolling element speed is chosen because it reflects the kinematics of the rolling element, particularly the rolling of the rolling element over the deformed outer ring. In steady-state conditions, it is expected that the rolling element speed will remain constant within the limits of numerical accuracy. Second, the internal load distribution and again the rolling element speed of the complete spherical roller bearing models are evaluated (see Section 3.2.2). Due to the recursive dependence of the internal load distribution and the deformation of the outer ring, the internal load distribution is suitable to verify the contact search and the contact force calculation between the rigid rolling elements and the deformed outer ring. When analyzing the rolling element speed, it is important to consider the physical acceleration and deceleration of the rolling elements within one rotation of the cage. Thirdly, the load distribution and the rolling element speed of the plummer block housing models are investigated to evaluate the method's capability to account for bearing surroundings with inhomogeneous stiffness distributions (see Section 3.2.3).

The reference solutions for the radial ring deflection are (1) an analytical solution according to Harris and Kotzalas [2], which is based on the theory of curved Timoshenko beams, and (2) the result of a linear static finite element simulation of the non-reduced model. The latter was modeled in Abaqus CAE/2023 and is identical to the single contact model shown in Fig. 8, but without

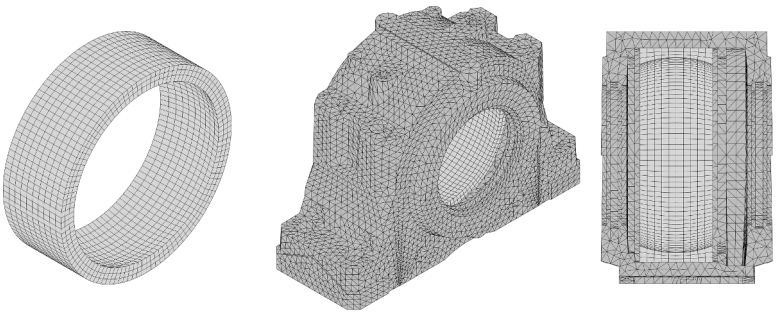

Fig. 11. Finite element models: (a) outer ring of the spherical roller bearing 22328-E1-XL and (b) split plummer block housing SNS3136 (dark gray) with outer ring (light gray).

rotation of the ring. The reference solutions for the internal load distributions were determined using Schaeffler's quasi-static bearing calculation program Bearinx, which is validated against experiments and finite element simulations [1,89]. Bearinx was chosen for two reasons: (1) To the best of the authors' knowledge, there is no comparable and accessible multibody simulation program for rolling bearings with elastic bearing surroundings, including the bearing rings. (2) It can be ensured that the internal bearing geometry, which has a significant impact on the load distribution, is consistent in the Caba3D and Bearinx models. The latter cannot be guaranteed in other programs, such as MESYS Rolling Bearing Calculation [101]. In Bearinx, cages and friction forces are neglected. The contact calculation is based on the slice model of ISO 16281 [88]. The stiffness of the bearing surroundings is incorporated as finite element-based influence numbers [1,89,102]. These numbers represent the local compliance of reference points located at the positions of the rolling elements and coupled to finite element nodes of the bearing ring cross-section [102]. Based on the finite element models shown in Fig. 11, the influence numbers were calculated using Abaqus CAE/2023. For the rolling element speed, no external reference solutions are used. The reasons are similar to those for choosing Bearinx, and, in addition, the rolling element speed over time is a dynamic process. Therefore, the rolling element speeds of the models with elastic bearing surroundings are compared with those of the corresponding rigid models.

Various results $x_{i,\mathrm{Caba3D}}$ of Caba3D are evaluated relative to different reference solutions $x_{i,\mathrm{ref}}$. Therefore, the relative error ε_i is defined as

$$\varepsilon_i = \frac{|x_{i,\mathrm{ref}} - x_{i,\mathrm{Caba3D}}|}{|x_{i,\mathrm{ref}}|}, \tag{25}$$

the maximum relative error $\varepsilon_{\max}$ as

$$\varepsilon_{\max} = \max_{i=1,\cdots,n} (\varepsilon_i), \tag{26}$$

and the mean relative error $\varepsilon_{\mathrm{mean}}$ as

$$\varepsilon_{\mathrm{mean}} = \frac{1}{n} \sum_{i=1}^{n} \varepsilon_i. \tag{27}$$

The time at which the results are evaluated differs between the models. For the single contact model and operating state 1 ($n_{\mathrm{IR}} = 0\ \mathrm{min}^{-1}$) of the spherical roller bearing model, evaluation is performed as soon as steady-state conditions are reached. For the remaining models, the overall frictional torque, which combines the frictional forces and torques of all contacts into a single integral parameter, is used as the convergence criterion (see Figs. 14 and 20). To improve convergence, the final states of the rigid models are selected as the initial states of the corresponding models with elastic bearing surroundings. A state is characterized by the positions,

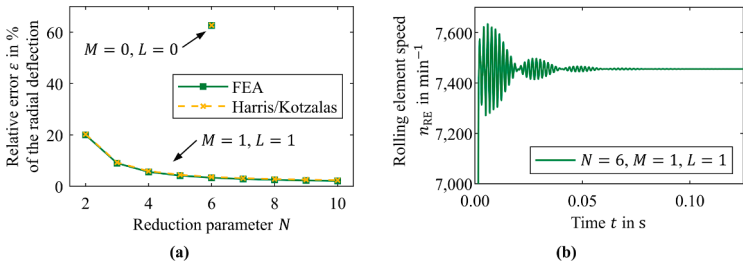

Fig. 12. Single contact model between rolling element and outer ring: (a) Relative error of the radial ring deflection at the position of the rolling element and (b) rolling element speed.

velocities, and accelerations of the rolling bearing components.

3.2. Results

3.2.1. Single contact model between rolling element and outer ring

The single contact model shown in Fig. 8 is first evaluated. Fig. 12(a) visualizes the results of the radial ring deflection at the position of the rolling element. The results for $M = 1$ and $L = 1$ converge towards the reference solutions as N increases. From $N = 5$ onwards, the relative error ε is less than 5%. Rigid modeling of the raceway cross-section ($M = 0$ and $L = 0$) is not sufficient, as indicated by the relative error $\varepsilon = 63\%$ for $N = 6$, $M = 0$, and $L = 0$. Instead, it is required that the deformation of the raceway cross-section is superimposed by linear Chebyshev polynomials ($M = 1$ and $L = 1$, see Eqs. (2) and (14)).

The rolling element speed n_{RE} over time t is shown in Fig. 12(b). Initially, the rolling element accelerates before settling at a constant speed after $t \approx 0.1$ s. Thus, the rolling element rolls continuously over the deformed outer ring in steady-state conditions.

3.2.2. Spherical roller bearing model

Following the single contact model, the complete spherical roller bearing model, as shown in Fig. 9, is investigated. To determine the influence of the reduction parameter N, a parameter study is first performed using operating state 1 as an example. The values $M = 1$ and $L = 1$ are based on the results of the single contact model (see Fig. 12(a)). Fig. 13 shows the load distribution between the rolling elements and the elastic outer ring for different values of N. The normal force $\overline{F}_{\mathrm{n}}$ is normalized to the maximum normal force when the outer ring is rigid. As N increases, the load distribution converges towards the Bearinx reference solution. The results are in good agreement for $N \geq 4$. The maximum relative error $\varepsilon_{\max}$ is 8.0% for $N = 4$ and decreases to 6.6% for $N = 6$. The mean relative errors $\varepsilon_{\mathrm{mean}}$are 3.0% for $N = 4$ and 2.6% for $N = 6$. Furthermore, the maximum normal force is approximately 15% lower when the outer ring is modeled as an elastic rather than a rigid body.

Based on the parameter study, the remaining operating states were simulated with $N = 6$, $M = 1$, and $L = 1$. As mentioned in Section 3.1, the frictional torque is used to determine the evaluation period. Fig. 14 shows the frictional torque over time for operating state 2 as an example. Once the frictional torque converges, the evaluation period corresponds to one rotation of the cage, meaning each rolling element passes through the load zone once. In the following, the normal force $\overline{F}_{\mathrm{n}}$ and the rolling element speed $\overline{n}_{\mathrm{RE}}$ are each normalized to the maximum value of the operating states when the outer ring is rigid. This simplifies comparisons between elastic and rigid modeling and between operating states. The normal force is at its maximum in operating state 1, while the rolling element speed is at its maximum in operating state 4.

Fig. 15 shows the load distribution and the rolling element speed for operating state 2. The relative errors ε_i in the load distributions between Caba3D and Bearinx are less than 4%. Compared to the rigid ring, the outer ring's deformation results in a broader load zone and a more uniform load distribution. This is also the reason for the lower maximum normal force in Fig. 13 and the 38% higher mean frictional torque over the evaluation periods in Fig. 14. The rolling element speed is qualitatively similar for elastic and rigid outer rings. As soon as the rolling elements enter the load zone, they are accelerated and then continue moving at almost constant speed. At the end and outside the load zone, they are slowed down again. For the elastic outer ring, rolling elements accelerate earlier and decelerate later due to the broader load zone.

The reduced elastic coordinates are investigated in Fig. 16 for operating state 2. Figs. 16(a) and (b) show the time dependence of the reduced elastic coordinates. The analysis of the Fourier coefficient $a_{r,1,1,1}$ in the frequency domain (see Fig. 16(c)) proves that the oscillations are caused by physical factors. The dominant frequencies are the rotational frequency $f_{\mathrm{c}} \approx 8$ Hz of the cage and twice the over-rolling frequency $2f_{\mathrm{o}} \approx 227$ Hz of the rolling elements on the outer ring. As the two rolling element rows are arranged non-parallel in the circumferential direction, i.e., with an angular offset, the amplitude of $2f_{\mathrm{o}}$ is much greater than the amplitude of f_{o}.

The additional axial force in operating state 3 compared to operating state 2 causes deviations between the rolling element rows, as illustrated in Fig. 17. Rolling element row 2 is subjected to higher loads because the axial force is applied in the direction of row 2. Consequently, the load zone is broader and the maximum normal force $\overline{F}_{\mathrm{n}}$ is higher. For both rolling element rows, the relative errors ε_i in the load distributions between Caba3D and Bearinx are less than 5%. The differences in load distribution are also reflected in the rolling element speeds, as the rolling elements of row 1 are accelerated later and decelerated earlier due to the shorter load zone. Compared to the model with rigid outer ring, the load zones of both rolling element rows are broader because of the deformation of the

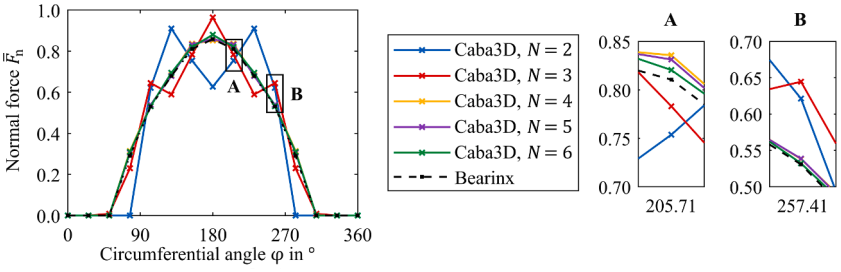

Fig. 13. Influence of the reduction parameter N on the load distribution of the spherical roller bearing 22328-E1-XL, rolling element row 2, for operating state 1 with reduction parameters N = var., $M = 1$, and $L = 1$.

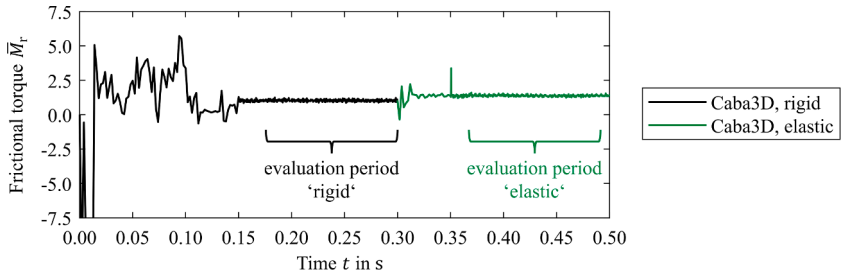

Fig. 14. Frictional torque of the spherical roller bearing 22328-E1-XL, operating state 2, with reduction parameters $N = 6$, $M = 1$, and $L = 1$. The values are relative to the mean frictional torque during the evaluation period 'rigid'. Restart of the simulation with elastic outer ring at $t = 0.30$ s.

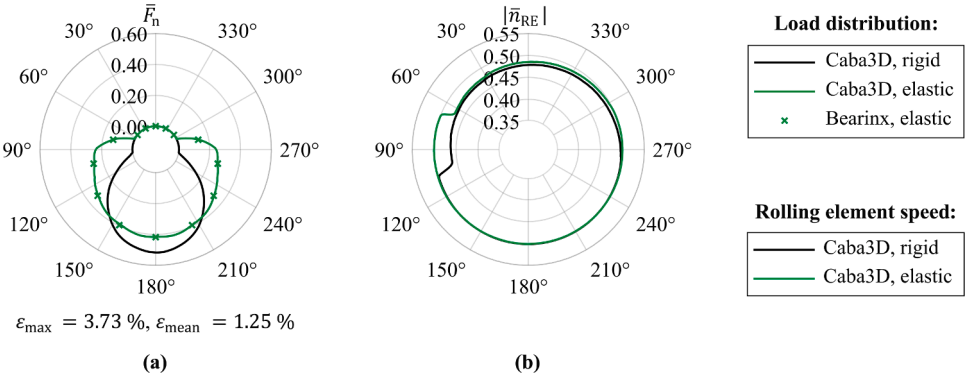

Fig. 15. Operating state 2 of the spherical roller bearing 22328-E1-XL, rolling element row 2: (a) load distribution and (b) rolling element speed with reduction parameters $N = 6$, $M = 1$, and $L = 1$.

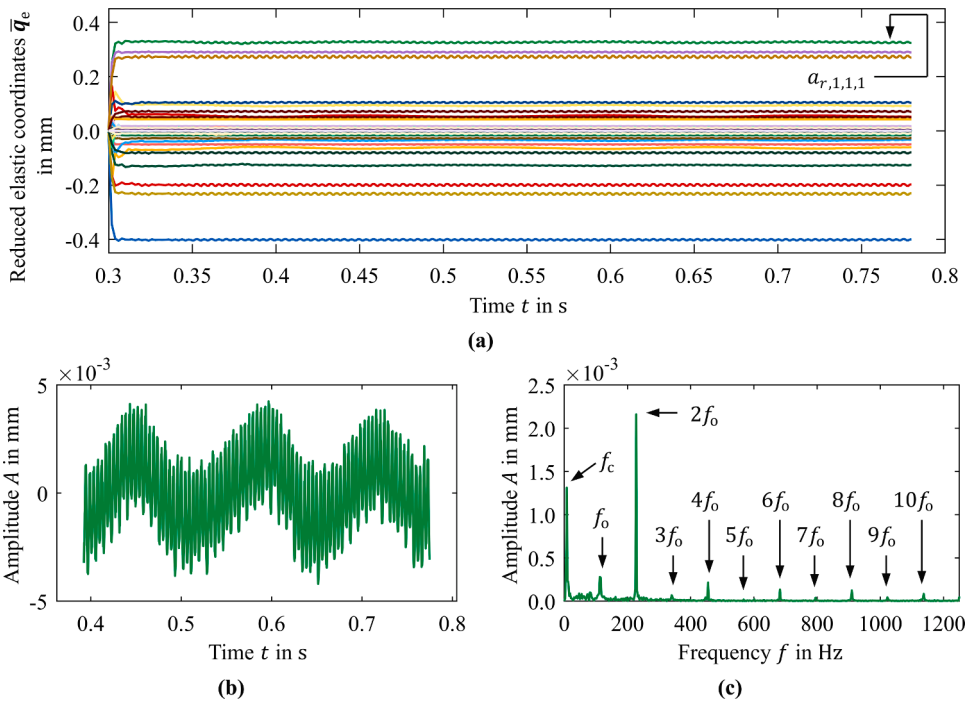

Fig. 16. Reduced elastic coordinates of the spherical roller bearing 22328-E1-XL for operating state 2 with reduction parameters $N = 6$, $M = 1$, and $L = 1$: (a) all reduced elastic coordinates, (b) detailed view of $a_{r,1,1,1}$ in the time domain, and (c) in the frequency domain.

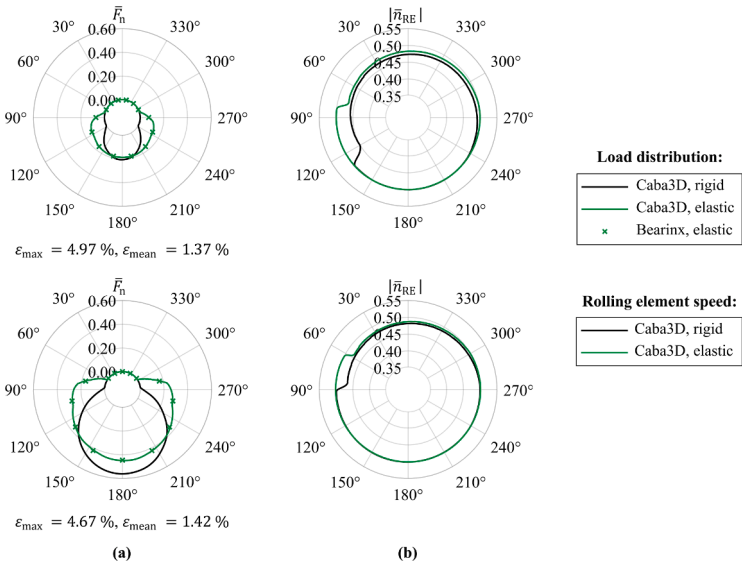

Fig. 17. Operating state 3 of the spherical roller bearing 22328-E1-XL, rolling element row 1 (top) and row 2 (bottom): (a) load distribution and (b) rolling element speed with reduction parameters $N = 6$, $M = 1$, and $L = 1$.

elastic outer ring. As a result, the rolling elements in both rows are accelerated earlier and decelerated later.

The load distribution and the rolling element speed for operating state 4 are shown in Fig. 18. The results are similar to those for operating state 2. As the radial force in operating state 4 is slightly reduced, the forces acting on the rolling elements are also smaller. Furthermore, the rolling element speed is significantly higher than in operating state 2 because the inner ring runs at twice the speed.

In addition to the quality of the results, the computation time is crucial for the application of the developed method. Therefore, Fig. 19 evaluates the relative computation time and the relative errors in the load distribution using operating state 5 as an example. The former is defined as the computation time for the model with elastic bearing surroundings relative to the computation time for the rigid modeled bearing. Both the relative computation time and the relative error depend on the reduction parameter N, which is varied from $N = 3$ to $N = 6$. As expected, the relative errors decrease with larger values for N, while the computation time increases. $N = 4$ is sufficient for $\varepsilon_{max} < 10\%$, $N = 5$ is required for $\varepsilon_{max} < 5\%$, and $N = 6$ for $\varepsilon_{max} < 2\%$. The relative computation time increases from 3.4 for $N = 4$ to 4.7 for $N = 6$.

3.2.3. *Plummer block housing model*

Figs. 21–23 show the load distributions and the rolling element speeds for all operating states of the spherical roller bearing mounted in the plummer block housing. Based on Sections 3.2.1 and 3.2.2, the finite element model of the housing, including the outer ring, was reduced using the parameters $N = 6$, $M = 1$, and $L = 1$. The normal force $\bar{F}_n$ is normalized to the maximum normal force of operating state 3 (rigid outer ring), which is the maximum normal force of all rigid models. The rolling element speed $\bar{n}_{RE}$ is normalized to the corresponding maximum rolling element speed of operating state 3. The evaluation period corresponds again to one rotation of the cage and is determined based on the frictional torque, as illustrated in Fig. 20 for operating state 1. The mean frictional torque is

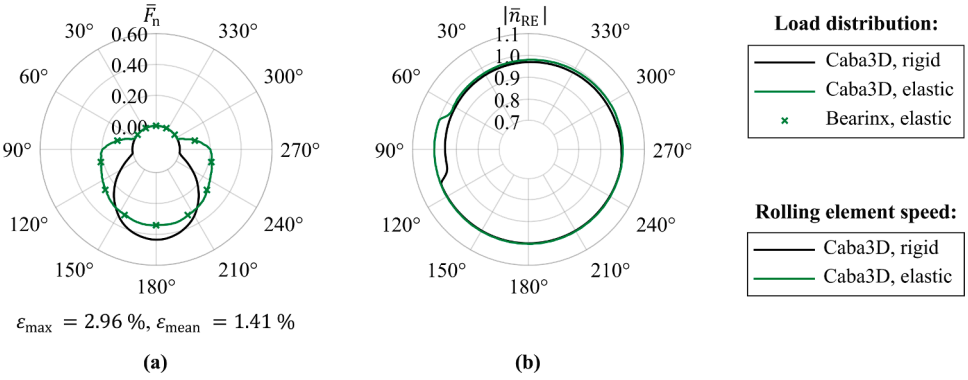

Fig. 18. Operating state 4 of the spherical roller bearing 22328-E1-XL, rolling element row 2: (a) load distribution and (b) rolling element speed with reduction parameters $N = 6$, $M = 1$, and $L = 1$.

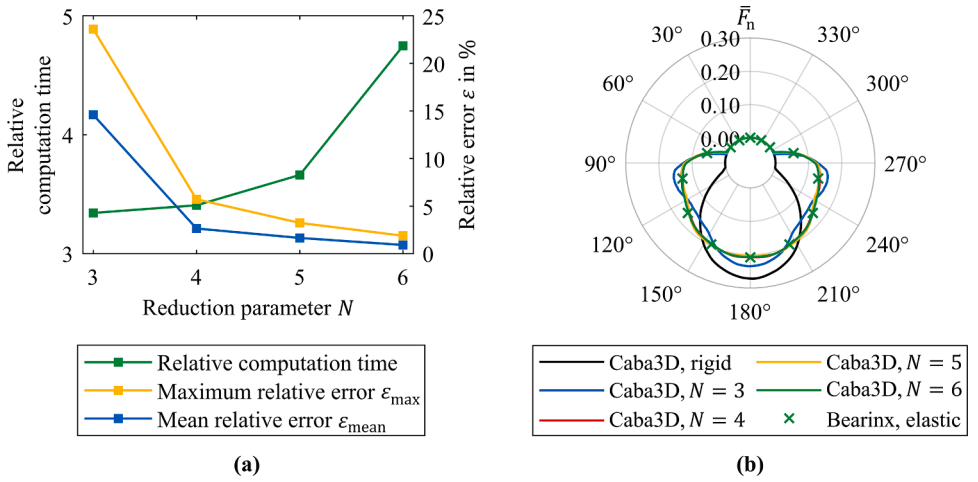

Fig. 19. Operating state 5 of the spherical roller bearing 22328-E1-XL: (a) relative computation time and (b) load distribution of rolling element row 2 with reduction parameters N = var., $M = 1$, and $L = 1$.

21% higher during the 'elastic' than during the 'rigid' evaluation period.

The normal forces $\overline{F}_n$ deviate by a maximum of $\varepsilon_{mean} = 3.68\%$ (operating state 4, row 1). In contrast to the results of Section 3.2.2, the maximum errors ε_{max} are above 5% for several operating states. The maximum error is 10.27% (operating state 5). However, as the largest errors always occur at the ends of the load zone, where the normal force $\overline{F}_n$ is considerably lower than in the center, these errors are less significant than those in the center. For example, in operating state 5, the maximum normal force $\overline{F}_n$ of the reference solution is 5.3 times greater than the normal force at the ends of the load zone, where an error of 10.27% occurs.

The rolling element speeds $\overline{n}_{RE}$ of the elastic housings are consistent with the corresponding rolling element speeds $\overline{n}_{RE}$ of the rigid models, taking into account the influence of the elastic deformations as explained below. Within the load zone, the rolling elements move at an almost constant speed in all operating states.

For rigid plummer block housings, the normal forces $\overline{F}_n$ and the rolling element speeds $\overline{n}_{RE}$ differ in the three load directions $\alpha = 180°$, 235°, and 270°, as the external force F_{IR} varies. However, the qualitative distributions are almost identical, as minor deviations only result from the different load directions relative to the gravitational acceleration. The internal bearing dynamics of the elastic housing, on the other hand, depend significantly on the load direction.

When the radial component of the external force is applied at $\alpha = 180°$, the load is distributed more uniformly compared to the rigid models (see Fig. 21). For example, in operating state 1, the maximum normal force $\overline{F}_n$ is 14.4% lower with a $\pm 4°$ broader load zone. As expected, the rolling elements are accelerated earlier and decelerated later.

For the load direction $\alpha = 235°$, the rolling elements are accelerated later and decelerated earlier due to the smaller load zone (see Fig. 22). For example, in operating state 3, the rolling elements enter the load zone 6° later and exit 2.5° earlier. At the same time, the maximum normal force $\overline{F}_n$ is 10.1% greater. The reason for the smaller load zone is the higher compliance of the housing at $\alpha = 180°$ and $\alpha = 270°$ compared to $\alpha = 235°$ (see Fig. 10), which allows the elastic outer ring to adapt to the rolling element row.

The influence of elastic modeling on the internal bearing dynamics is particularly evident in Fig. 23 for the load direction $\alpha = 270°$. Since the upper half of the plummer block housing is more compliant than the lower half, the load zones end significantly later. While the maximum normal forces $\overline{F}_n$ are similar, their locations differ. In operating state 5, for example, the rolling elements exit the load zone at 17° (elastic housing) compared to 349° (rigid housing), and the maximum normal force $\overline{F}_n$ is reached at 252° (elastic housing) compared to 271° (rigid housing).

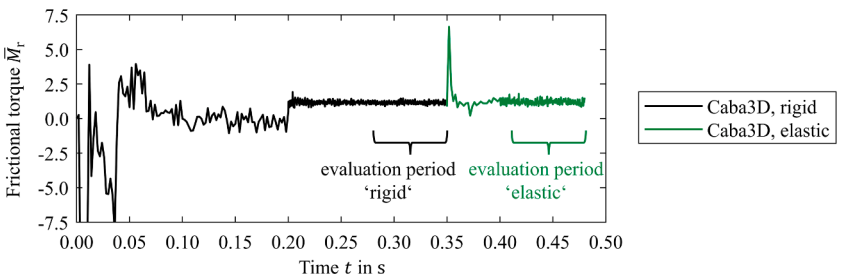

Fig. 20. Frictional torque of the spherical roller bearing 22328-E1-XL mounted in the plummer block housing SNS3136, operating state 1, with reduction parameters $N = 6$, $M = 1$, and $L = 1$. The values are relative to the mean frictional torque during the evaluation period 'rigid'. Restart of the simulation with elastic bearing surroundings at $t = 0.35$ s.

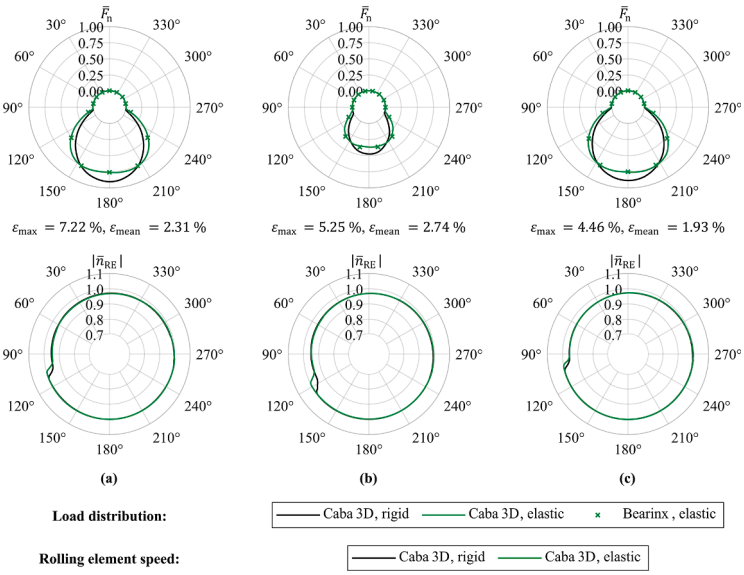

Fig. 21. Load distribution (top) and rolling element speed (bottom) of the spherical roller bearing 22328-E1-XL mounted in the plummer block housing SNS3136 for (a) operating state 1, rolling element row 2, (b) operating state 2, rolling element row 1, and (c) operating state 2, rolling element row 2 with reduction parameters $N = 6$, $M = 1$, and $L = 1$.

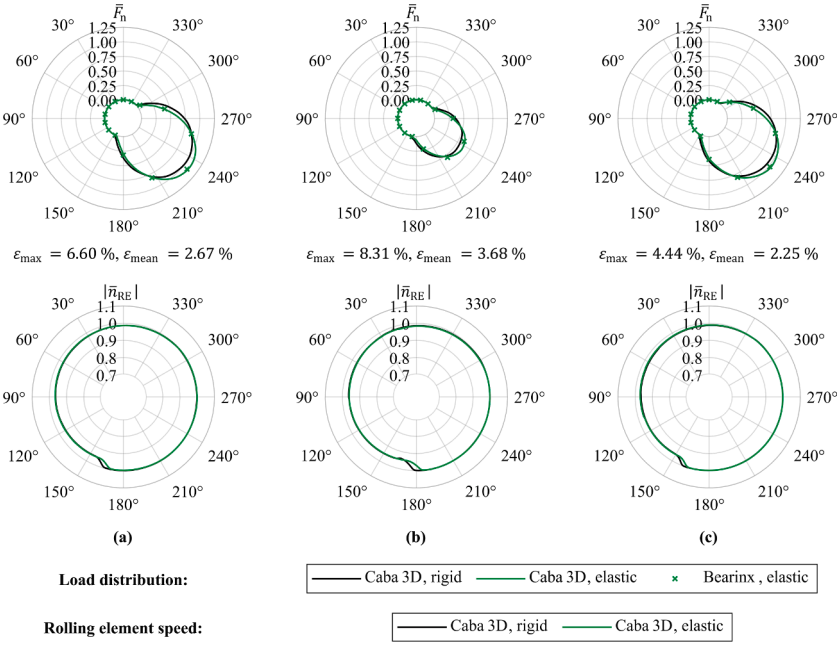

Fig. 22. Load distribution (top) and rolling element speed (bottom) of the spherical roller bearing 22328-E1-XL mounted in the plummer block housing SNS3136 for (a) operating state 3, rolling element row 2, (b) operating state 4, rolling element row 1, and (c) operating state 4, rolling element row 2 with reduction parameters $N = 6$, $M = 1$, and $L = 1$.

3.3. Discussion

To achieve aim (1) defined in Section 1, a new and reliable method for integrating the bearing surroundings as an elastic body into multibody simulation of rolling bearings at low computational cost has been successfully developed in Section 2. The method is verified for several spherical roller bearing models in Section 3.2. In the single contact model (see Section 3.2.1), errors of less than 5% in the radial ring deflection confirm the correct elastic modeling of the outer ring. In addition, the rolling element's constant speed under steady-state conditions demonstrates its continuous rolling over the deformed raceway. For the models in Sections 3.2.2 and

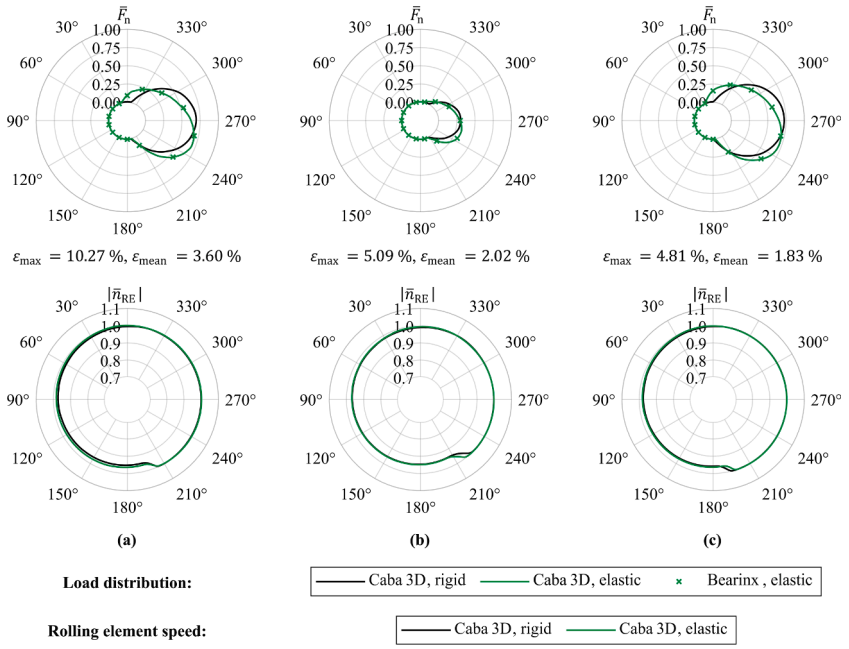

Fig. 23. Load distribution (top) and rolling element speed (bottom) of the spherical roller bearing 22328-E1-XL mounted in the plummer block housing SNS3136 for (a) operating state 5, rolling element row 2, (b) operating state 6, rolling element row 1, and (c) operating state 6, rolling element row 2 with reduction parameters $N = 6$, $M = 1$, and $L = 1$.

3.2.3, the load distributions deviate by $\varepsilon_{mean} < 4\%$ (see Fig. 22(b)), which verifies the contact search and force calculation between the rigid rolling elements and the deformed outer ring. Maximum errors ε_{max} of up to 10.27% (see Fig. 23(a)) can occur at the ends of the load zone, where the normal forces are considerably lower compared to the center. Due to the relative evaluation, minor deviations in the width of the load zone can result in disproportionately large relative errors at the ends of the load zone. However, since the absolute forces at the ends of the load zones are small, these errors have only a minor influence. As discussed in Section 3.1, Bearinx is a quasi-static calculation program with several simplifications compared to Caba3D. Therefore, the normal forces may also differ for this reason. In contrast, deviations are not caused by differences in geometry, material, or boundary conditions, as these are consistent in the Caba3D and Bearinx models. This consistency is the main reason why Bearinx was used to determine the reference solutions (see Section 3.1). The evaluation of the rolling element speed in Sections 3.2.2 and 3.2.3 confirms again the correct kinematics of the rolling elements, particularly the rolling of the rolling elements over the deformed outer ring. As a result, aim (2) has been successfully achieved.

The effects of external loads and operating speeds on the internal load distribution and the rolling element speed have been investigated in several studies for different types of rolling bearings. These investigations include analytical approaches [1,2,103], numerical simulations [3,5,6,13,26,52,66,78,80], and experimental analyses [104,105]. The results from Section 3.2 are consistent with the findings of these studies regarding the maximum load, the width of the load zone, and the acceleration and deceleration of the rolling elements. As mentioned in Section 2.5, Caba3D is validated for rigid bearing surroundings against experiments [97–99] and simulations [42,43,45,91]. The influence of elastic bearing surroundings, including different bearing ring thicknesses and housing designs, on the internal load distribution has been addressed in [1–3,5,6,66,78,80]. The results presented in Section 3.2 are again in good agreement with the conclusions drawn in these references.

The proposed method is computationally efficient because the elastic modeling of bearing surroundings adds only a few additional degrees of freedom. In Section 3.2, the finite element models were reduced with $N = 6$, $M = 1$, and $L = 1$ to 156 degrees of freedom. Although this number exceeds the six degrees of freedom of a rigid body, it is significantly fewer than the thousands or millions of degrees of freedom of a non-reduced finite element model. Furthermore, the efficient analytical contact search for rigid models described in [43] is no longer applicable due to the more complex representation of the deformed raceway according to Eq. (15), which replaces the simpler description of the undeformed raceway given in Eq. (13). Consequently, the contact search must be performed numerically, as outlined in Section 2.4.2. The computation time analysis presented in Fig. 19 shows that a simulation including elastic bearing surroundings requires approximately three to five times more computation time than a simulation with only rigid components. Considering the higher model quality, the authors deem this increase in computation time acceptable.

In contrast to Wensing [84], fixed interface normal modes were not used for the reduction of the finite element model, as the deformation of the interface (i.e., the raceway) is determined by the modes introduced in Section 2.1. Fixed interface normal modes only describe the dynamic behavior of the internal structure [72,84,106]. Although their influence was not explicitly investigated in this study, the good results in Section 3.2 suggest only a minor dependency in the models simulated. Incorporating fixed interface normal modes in the reduction of the finite element model could further improve the quality of the results, while also increasing the

degrees of freedom.

The results obtained for the plummer block housing in Section 3.2.3 show that the method can account for inhomogeneous stiffness distributions of real bearing surroundings. However, the proposed method may be limited in bearing surroundings with highly variable stiffness. This may be achieved to a certain extent by increasing the values for N, M, and L, while simultaneously increasing the degrees of freedom. To evaluate the effectiveness of this method in highly variable stiffness distributions, further research is required.

Since the finite element meshes of the bearing rings and their surrounding components are tied and modeled as one elastic body in the multibody simulation, relative motions between the elastic components are not possible. Therefore, effects such as bearing creep are neglected. Modeling the components as separate bodies enables the effects in the contact joint to be resolved more accurately. However, this increases the degrees of freedom and requires an additional contact calculation, which also increases the computation time.

The proposed method is described as an example for the outer ring of a spherical roller bearing. However, it can also be applied to the inner ring and other types of rolling bearings. To this end, the profile $\boldsymbol{p}(u)$ (see Eq. (12)) must be substituted with the actual contact geometry of the respective bearing ring. For instance, the raceway profile of a tapered roller bearing corresponds to a straight line inclined with respect to the bearing axis, whereas the raceway profile of a deep groove ball bearing is a circular arc segment. Depending on the type of roller bearing, the contact calculation must also be extended, for example by employing alternative contact force models or by accounting for rib contact interactions.

To summarize, the following future research directions regarding the proposed method have been identified:

- Experimental validation of the proposed method.
- Analysis of the influence of fixed interface normal modes on the dynamic bearing behavior and the computation time.
- Performance evaluation of the developed method for bearing surroundings with highly variable stiffness distributions, e.g., cooling fins.
- Application of the method to the inner ring and other types of rolling bearings.
- Extension of the contact calculation by improved slicing techniques [24,92], contact force models for elastic bodies, and contact interactions between rolling elements and ribs.
- Investigations of contact interactions between components of the elastic bearing surroundings, such as meshing between gears or bearing creep.

4. Effects of elastic bearing surroundings on vibrations

To further investigate the effects of elastic surroundings, a case study on the vibration response of the inner ring was conducted.

4.1. Case study setup

The spherical roller bearing 22328-E1-XL is again chosen as an example. The inner ring rotates at constant speed $n_{\mathrm{IR}} = 2,420\ \mathrm{min}^{-1}$ and is loaded with the radial force $F_{\mathrm{r}} = 430$ kN. The surroundings are varied as follows:

- Case (1): rigid outer ring (see operating state 4, Section 2.6.2, and operating state 1, Section 2.6.3)
- Case (2): elastic outer ring (see operating state 4, Section 2.6.2)
- Case (3): elastic plummer block housing and outer ring (see operating state 1, Section 2.6.3)

Based on the results of Section 3.2, the finite element models of cases (2) and (3) were reduced using the parameters $N = 6$, $M = 1$, and $L = 1$.

4.2. Results

Fig. 24 shows the displacements of the inner ring's center in the y- and z-direction (see Figs. 9 and 10) for one rotation of the cage ($\Delta t \approx 0.0625$ s). The initial position of the inner ring is at $(x,y) = (0,0)$. In all three cases, the displacements are composed of quasi-constant shifts in the positive y- and z-directions and additional high-frequency movements. The shift in the y-direction results from the radial force and gravity acting in that direction. The rotation of the rolling element rows causes the shift in the z-direction and the high-frequency movements in both directions. The magnitudes of the shifts and movements depend on the stiffness of the surroundings. As the elastic outer ring is the most flexible, the inner ring experiences the largest shifts and movements in case (2). In contrast, the inner ring is displaced the least in case (1), because the outer ring is modeled as a rigid body.

The frequencies of the inner ring's displacements are analyzed in Fig. 25. The spectra are primarily characterized by the rotational frequency $f_{\mathrm{c}} \approx 16$ Hz of the cage, the over-rolling frequency $f_{\mathrm{o}} \approx 227$ Hz of the rolling elements on the outer ring, and their higher-order harmonics. The amplitudes of these frequencies, however, differ significantly among the three cases. The rotational frequency f_{c} of the cage is present in all cases. In case (1), the second harmonic $2f_{\mathrm{o}}$ dominates, since the two rolling element rows are arranged non-parallel in the circumferential direction, i.e., with an angular offset. In case (2), additional higher-order harmonics of f_{o}, namely $4f_{\mathrm{o}}$ and $6f_{\mathrm{o}}$, are excited, since the outer ring is elastic, but additional surrounding components, such as a housing, do not restrict its vibrations. Compared to cases (1) and (2), the main characteristics of case (3) are the high amplitudes of f_{o} and $3f_{\mathrm{o}}$ in addition to $2f_{\mathrm{o}}$. This effect results from the cage, which is composed of two unconnected halves, and the geometry of the plummer block housing. As

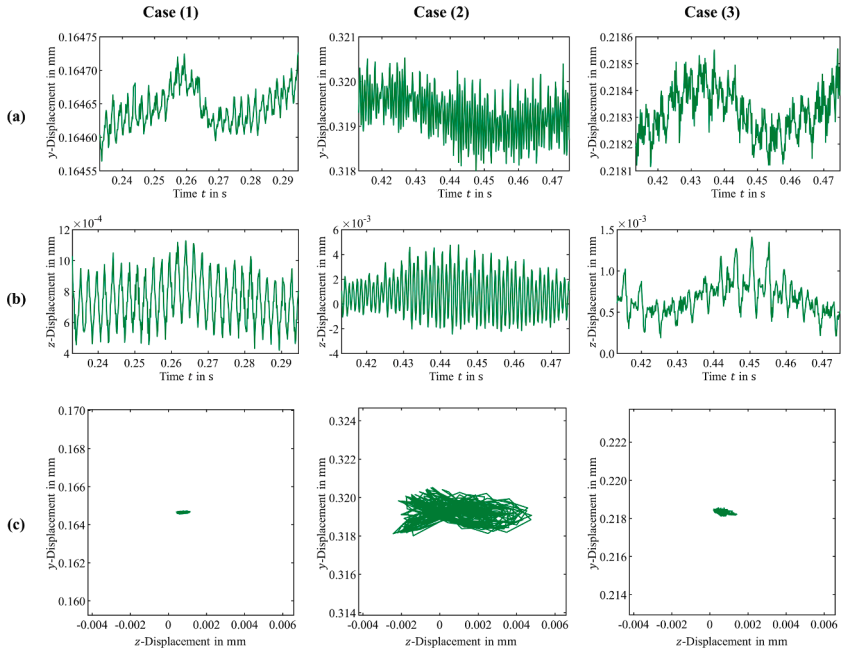

Fig. 24. Vibration response of the inner ring's center in the time domain for case (1) (left), case (2) (center), and case (3) (right): (a) y-displacement, (b) z-displacement, and (c) trajectory.

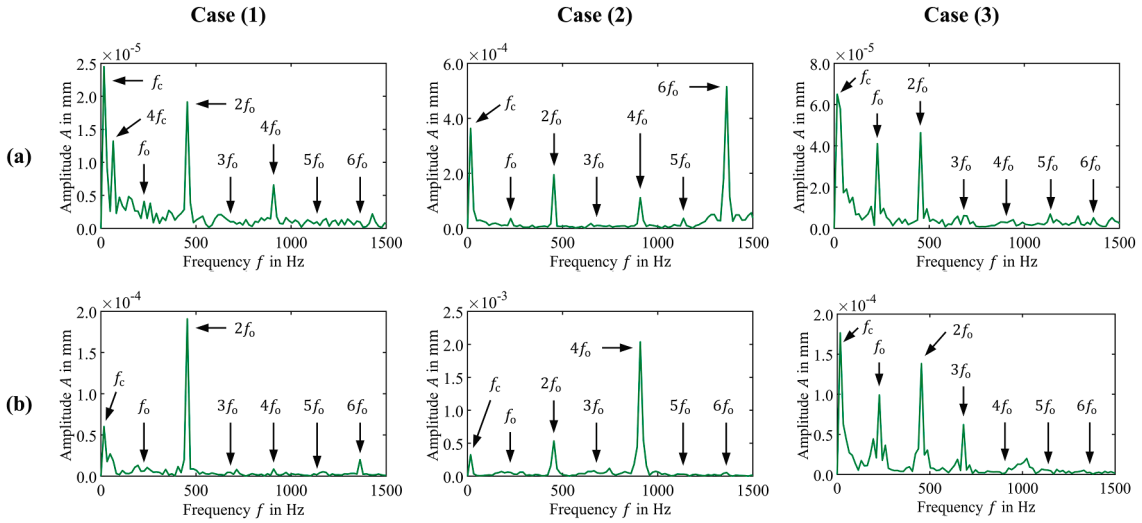

Fig. 25. Vibration response of the inner ring's center in the frequency domain for case (1) (left), case (2) (center), and case (3) (right): (a) y-displacement and (b) z-displacement.

shown in Fig. 11(b), the housing's geometry, and consequently its stiffness, is not symmetric in the axial direction, in contrast to the outer ring. Small asymmetrical deformations of the housing induce minor deviations in the load distributions among the rolling element rows, which in turn lead to slight differences in the rolling element speeds between the two rows. This changes the initial offset in the angular position between the rows over time. As a result, in addition to $2f_o$, the displacement of the inner ring is also

Table 5
Root mean square value of the inner ring's accelerations in m/s^2.

Direction	Case (1)	Case (2)	Case (3)
y	0.683	29.025	5.442
z	5.673	49.239	6.276

superimposed by f_o and $3f_o$ components.

As shown in Fig. 24, the inner ring moves more during one cage rotation in cases (2) and (3) than in case (1). This behavior affects the root mean square (RMS) values of the inner ring's accelerations in both directions, as proven in Table 5. Consistent with the movement of the inner ring, the RMS values increase from case (1) to case (3) and further to case (2). Overall, the elastic bearing surroundings have a greater influence on the RMS values in the *y*-direction than in the *z*-direction.

4.3. Discussion

In the case study, vibrations are induced by continuous changes in the angular positions of the rolling elements with respect to the direction of the external load. This causes periodic displacements of the inner ring in the vertical and horizontal directions. In single row rolling bearings, the primary frequency of vibration corresponds to the over-rolling frequency f_o of the rolling elements [1,103]. In the case study, however, the two rolling element rows of the spherical roller bearing are arranged with an angular offset in the circumferential direction, so that the second harmonic $2f_o$ dominates over f_o. Furthermore, the displacements of the inner ring are affected by the rotational frequency f_c of the cage, as the rolling elements are guided by the cage.

The displacements of the inner ring and the RMS values of its accelerations indicate a significant influence of the surrounding stiffness on the vibration behavior of the rolling bearing. Note that the elastic outer ring of case (2) represents a rather theoretical example, as the outer ring is generally mounted in a housing or gear body. Consequently, the absolute values of case (2) are likely overestimated compared to practical rolling bearing applications. This statement is also supported by the results of the plummer block housing (see case (3)). Moreover, the shaft was neglected in all three models, and it is expected that its mass and inertia can also affect the absolute vibration behavior of the rolling bearing.

In contrast to the case study, the influence of defects in bearing rings and rolling elements on the vibrations of rolling bearings have been analyzed in several numerical and experimental investigations, for example, in [50,75,76,83,107–109]. Depending on several factors, such as the type, shape, and location of the defects, the vibration amplitude generally increases with the defect size, as the operating clearance increases. For instance, Kogan et al. [50] found that the displacements and accelerations of the inner ring increase with the size of the defect in the outer ring. Similar conclusions were reported in [76,83,107,108] and for defective rolling elements in [75,108,109]. However, He et al. [75] observed for defective rolling elements that the vibration amplitude increases with the defect width but remains unchanged with the defect depth. The results presented in Section 4.2 are consistent with these conclusions, as the deformation of the outer ring increases the operating clearance in the direction of the external load, which in turn leads to larger radial displacements and consequently higher accelerations of the inner ring. In [75], the defect depth of the rolling element does not influence the operating clearance of the rolling bearing, and therefore, this finding does not contradict the present results.

The purpose of the case study was to concisely investigate the effects of elastic bearing surroundings on the vibration response of the inner ring. A detailed analysis of the dynamic performance is beyond the scope of the case study. As a roadmap for future extensions of the case study, the vibration behavior can be evaluated both numerically and experimentally, considering the effects of external loads, operating speeds, alternative bearing surroundings, and defects in the rolling elements and bearing rings.

5. Conclusions

A new, verified, and computationally efficient method for integrating bearing surroundings (e.g., housing, gear body, or shaft including the bearing rings) as an elastic body into multibody simulation of rolling bearings has been proposed. The derived 3D dynamic roller bearing models have several advantages over models of the current state of research:

- The bearing rings and their inner contact surfaces can deform elastically, rather than performing only rigid body motions.
- The method can account for inhomogeneous stiffness distributions of bearing surroundings and is not limited to simple structures with rotational and axial symmetry.
- Elastic deformations are neither calculated in advance of the multibody simulation for selected operating states using finite element analyses, nor specified by a predefined Fourier series. Instead, the bearing rings deform dynamically according to the external loads and internal load distribution, making the elastic modeling independent of the operating state.
- The continuous description of the deformed contact surfaces, which is required for the contact calculation, is an integral part of the elastic modeling, eliminating the need to reconstruct the deformed contact surfaces (e.g., with splines).
- The rolling elements roll continuously over the deformed bearing rings without being coupled to them, depending on the position of the rolling elements (e.g., with spring-damper elements).
- The method is described as an example for the outer ring of a spherical roller bearing. However, it can also be applied to the inner ring and other types of rolling bearings.

The results confirm the hypothesis that the stiffness of bearing surroundings can influence the internal dynamic behavior of rolling bearings. Both the internal load distribution and the rolling element speed can change due to elastic deformations of the bearing surroundings. The mean frictional torque increases as a result of broader load zones. Furthermore, elastic deformations of the outer ring can increase the operating clearance of the rolling bearing in the direction of the external load, which leads to larger radial displacements and thus higher accelerations of the inner ring.

Nomenclature

The following symbols are used in this manuscript:

Symbol	Unit	Description
a	mm	Length base of the housing
A	mm	Amplitude
$\boldsymbol{a}_k$	–	Fourier coefficients, $k \in \{x,r,t\}$
$a_{k,n,m,l}$	–	Fourier coefficient, $k \in \{x,r,t\}$, $n \in \{0,\cdots,N_k\}$, $m \in \{0,\cdots,M_k\}$, $l \in \{0,\cdots,L_k\}$
b	–	Boundary degrees of freedom
B	mm	Width of the bearing
$\boldsymbol{b}_k$	–	Fourier coefficients, $k \in \{x,r,t\}$
$b_{k,n,m,l}$	–	Fourier coefficient, $k \in \{x,r,t\}$, $n \in \{1,\cdots,N_k\}$, $m \in \{0,\cdots,M_k\}$, $l \in \{0,\cdots,L_k\}$
C_{0r}	kN	Radial basic static load rating of the rolling bearing
c_1, c_2	–	Parameters of the contact normal force calculation
c_{d1}, c_{d2}	–	Parameters of the material damping force calculation
C_r	kN	Radial basic dynamic load rating of the rolling bearing
${}^{R}\boldsymbol{c}$	mm	Position of a point relative to K_R expressed in K_R, $\mathbb{R}^3$
d	mm	Distance between slice center and raceway
d	mm	Bore diameter of the rolling bearing
D	mm	Outside diameter of the rolling bearing
$\boldsymbol{D}_e$	Ns/mm	Damping matrix, $\mathbb{R}^{N_{FE}\times N_{FE}}$
$\overline{\boldsymbol{D}}_e$	Ns/mm	Reduced damping matrix, $\mathbb{R}^{n_{FE}\times n_{FE}}$
E	N/mm^2	Youngs modulus
F_a	kN	Axial force
f_c	Hz	Rotational frequency of the cage
$F_{c,n}$	N	Contact normal force per slice
$F_{d,m}$	N	Material damping force per slice
$F_{d,l}$	N	Lubricant damping force per slice
F_{IR}	kN	Force on the inner ring
$\overline{F}_n$	–	Normalized contact normal force
f_o	Hz	Over-rolling frequency on the outer ring
F_r	N	Friction force per slice
F_r	kN	Radial force
F_{RE}	kN	Force on the rolling element
g	mm	Housing width
h	N/A	Equality constraint
h_1	mm	Housing height
$\boldsymbol{h}_c$	N	Resulting contact force, $\mathbb{R}^3$
$\overline{\boldsymbol{h}}_c$	N	Resulting contact force, $\mathbb{R}^{n_{FE}}$
i	–	Internal degrees of freedom
$\boldsymbol{I}_{bb}$	N/A	Identity matrix, $\mathbb{R}^{N_b\times N_b}$
$\boldsymbol{K}_e$	N/mm	Stiffness matrix, $\mathbb{R}^{N_{FE}\times N_{FE}}$
$\overline{\boldsymbol{K}}_e$	N/mm	Reduced stiffness matrix, $\mathbb{R}^{n_{FE}\times n_{FE}}$
$\boldsymbol{K}_{ii}$	N/mm	Submatrix of $\boldsymbol{K}_e$, $\mathbb{R}^{N_i\times N_i}$
$\boldsymbol{K}_{ib}$	N/mm	Submatrix of $\boldsymbol{K}_e$, $\mathbb{R}^{N_i\times N_b}$
K_R	–	Reference coordinate system
L, L_k	–	Degree of the Chebychev polynomials T_l, reduction parameter, $k \in \{x,r,t\}$
l_c	mm	Contact length
l_s	mm	Slice length
M, M_k	–	Degree of the Chebychev polynomials T_m, reduction parameter, $k \in \{x,r,t\}$
$\boldsymbol{M}_e$	t	Mass matrix, $\mathbb{R}^{N_{FE}\times N_{FE}}$
$\overline{\boldsymbol{M}}_e$	t	Reduced mass matrix, $\mathbb{R}^{n_{FE}\times n_{FE}}$
$\overline{\boldsymbol{M}}_r$	–	Normalized frictional torque
$\boldsymbol{n}^{(0)}$	mm	Normalized normal of the slice plane, $\mathbb{R}^3$
N, N_k	–	Degree of the Fourier polynomials, reduction parameter, $k \in \{x,r,t\}$
N_b	–	Number of boundary degrees of freedom
$\boldsymbol{n}_c$	mm	Normalized contact normal, $\mathbb{R}^3$
n_{FE}	–	Number of degrees of freedom of the reduced elastic coordinates
N_{FE}	–	Number of degrees of freedom of the elastic coordinates
n_G	min^{-1}	Limiting rotational speed of the rolling bearing
N_i	–	Number of internal degrees of freedom
$\boldsymbol{n}_i$	mm	Normalized surface normal of slice i, $\mathbb{R}^3$
n_{IR}	min^{-1}	Rotational speed of the inner ring
n_{OR}	min^{-1}	Rotational speed of the outer ring
$\boldsymbol{n}_p^{(0)}$	mm	Normalized surface normal at $\boldsymbol{x}_p^{(0)}$, $\mathbb{R}^3$
$\boldsymbol{n}_p^{(1)}$	mm	Normalized surface normal at $\boldsymbol{x}_p^{(1)}$, $\mathbb{R}^3$
n_{RE}	min^{-1}	Rotational speed of the rolling element
$\overline{n}_{RE}$	–	Normalized rotational speed of the rolling element
n_s	–	Number of slices

(*continued on next page*)

(*continued*)

p	mm	Penetration between slice and raceway
$\boldsymbol{p}$	mm	Undeformed profile of the (contact) surfaces in parameter form, $\mathbb{R}^2$
$\dot{\boldsymbol{q}}_\mathrm{c}$	mm/s	Deformation velocity at the contact point, $\mathbb{R}^3$
$\boldsymbol{q}_\mathrm{e}$	N/A	Elastic coordinates, $\mathbb{R}^{N_\mathrm{FE}}$
$\overline{\boldsymbol{q}}_\mathrm{e}$	N/A	Reduced elastic coordinates, $\mathbb{R}^{n_\mathrm{FE}}$
R	mm	Radius of the raceway
$\overline{R}$	mm	Maximal radius of the raceway
r_i	mm	Radius of slice i
S	–	Safety factor
S_0	–	Static load safety factor of the rolling bearing
$\boldsymbol{s}_0$	mm	Undeformed (contact) surfaces in parameter form, $\mathbb{R}^3$
$\boldsymbol{s}_1$	mm	Deformed (contact) surfaces in parameter form, $\mathbb{R}^3$
t	s	Time
$\boldsymbol{T}$	–	Transformation matrix, $\mathbb{R}^{N_\mathrm{b}\times n_\mathrm{FE}}$
T_j, T_l, T_m	–	Chebyshev polynomials of degree j, l and m
$\boldsymbol{T}_k$	–	Submatrix of $\boldsymbol{T}$, $k \in \{x,r,t\}$, $\mathbb{R}^{N_\mathrm{b}\times n_{\mathrm{FE}_k}}$
$\boldsymbol{t}_\mathrm{p}^{(1)}$	mm	Normalized cross product of $\boldsymbol{n}^{(0)}$ and the vector from $\boldsymbol{x}_\mathrm{c}^{(0)}$ to $\boldsymbol{x}_\mathrm{p}^{(1)}$, $\mathbb{R}^3$
u	–	Parameter of $\boldsymbol{p}$ and first parameter of $\boldsymbol{s}_0$ and $\boldsymbol{s}_1$
$\boldsymbol{u}$	mm	Displacement, $\mathbb{R}^3$
u_k	mm	Displacement, $k \in \{x,r,t\}$
${}^\mathrm{R}\boldsymbol{u}$	mm	Displacement of ${}^\mathrm{R}\boldsymbol{c}$ expressed in $\mathrm{K_R}$, $\mathbb{R}^3$
v	–	Second parameter of $\boldsymbol{s}_0$ and $\boldsymbol{s}_1$
$\boldsymbol{V}_\mathrm{c}$	–	Coordinate transformation matrix (Guyan), constraint modes, $\mathbb{R}^{N_\mathrm{FE}\times N_\mathrm{b}}$
$\boldsymbol{V}_\mathrm{gc}$	–	Coordinate transformation matrix, global constraint modes $\mathbb{R}^{N_\mathrm{FE}\times n_\mathrm{FE}}$
$\widetilde{x}$	–	Argument of the Chebyshev polynomials
$\overline{X}$	mm	Half width of the raceway
$\boldsymbol{x}_\mathrm{c}$	mm	Contact point, $\mathbb{R}^3$
$\boldsymbol{x}_\mathrm{c}^{(0)}$	mm	Slice center, $\mathbb{R}^3$
$\boldsymbol{x}_{\mathrm{i},1}$, $\boldsymbol{x}_{\mathrm{i},2}$	mm	Intersection points between slice and raceway, $\mathbb{R}^3$
$\boldsymbol{x}_\mathrm{p}^{(0)}$	mm	Penetration point of the slice, $\mathbb{R}^3$
$\boldsymbol{x}_\mathrm{p}^{(1)}$	mm	Penetration point of the raceway, $\mathbb{R}^3$
(x,r,t)	mm	Axial, radial, and tangential directions
(x,r,φ)	mm, rad	Cylindrical coordinates
(x,y,z)	mm	Cartesian coordinates
α	°	Direction of the radial force F_r
Δv_n	mm/s	Relative velocity of the contact point in normal direction
ε_i	%	Relative error
ε_max	%	Maximal relative error
$\varepsilon_\mathrm{mean}$	%	Mean relative error
ν	–	Poisson's ratio
ρ	kg/dm^3	Density
$\boldsymbol{\Phi}$	N/A	Global shape matrix

Data availability

The source code and data on the simulation software Caba3D are not available due to trade secrets of Schaeffler Technologies AG & Co. KG. Raw simulation results are available upon reasonable request from the authors. The access to the simulation software Bearinx was thankfully provided by Schaeffler Technologies AG & Co. KG. Access to Bearinx is available upon request from Schaeffler Technologies AG & Co. KG and requires prior approval from Schaeffler Technologies AG & Co. KG.

CRediT authorship contribution statement

Tobias Baumann: Writing – original draft, Visualization, Validation, Software, Methodology, Investigation, Formal analysis, Data curation, Conceptualization. **Bodo Hahn:** Writing – review & editing, Validation, Software, Resources, Project administration, Data curation, Conceptualization. **Stephan Tremmel:** Writing – review & editing, Supervision, Resources, Project administration, Conceptualization.

Declaration of competing interest

The authors declare that they have no known competing financial interests or personal relationships that could have appeared to influence the work reported in this paper.

Acknowledgements

The authors would like to thank Schaeffler Technologies AG & Co. KG for permission to use the company's internal software Caba3D in the context of the research for this paper. Tobias Baumann and Stephan Tremmel greatly acknowledge the continuous support of the University of Bayreuth.

References

[1] Schaeffler Technologies AG, Co. KG, Ball and Roller Bearings: Handbook on the Design and Calculation of Rolling Bearing Arrangements, 2nd ed., Vereinigte Fachverlage, Mainz, Germany, 2022.
[2] T.A. Harris, M.N. Kotzalas, Advanced Concepts of Bearing Technology, 5th ed., CRC Press, Boca Raton, USA, 2023.
[3] T. Kiekbusch, Strategien zur dynamischen simulation von Wälzlagern, Ph.D. Thesis, Kaiserslautern, Germany, 2017.
[4] J. Torsvik, A.R. Nejad, E. Pedersen, Main bearings in large offshore wind turbines: development trends, design and analysis requirements, J. Phys. Conf. Ser. 1037 (2018) 42020, https://doi.org/10.1088/1742-6596/1037/4/042020.
[5] S. Kock, G. Jacobs, D. Bosse, Determination of wind turbine main bearing load distribution, J. Phys. Conf. Ser. 1222 (2019) 12030, https://doi.org/10.1088/1742-6596/1222/1/012030.
[6] G. Cavallaro, D. Nelias, F. Bon, Analysis of high-speed intershaft cylindrical roller bearing with flexible rings, Tribol. Trans. 48 (2005) 154–164, https://doi.org/10.1080/05698190590923851.
[7] Caba3D, An Insight into Rolling Bearing Dynamics, Schaeffler Technologies AG & Co. KG, Herzogenaurach, Germany, 2021.
[8] S.-W. Hong, V.-C. Tong, Rolling-element bearing modeling: a review, Int. J. Precis. Eng. Manuf. 17 (2016) 1729–1749, https://doi.org/10.1007/s12541-016-0200-z.
[9] R. Gismeros Moreno, F. Marques, E. Corral Abad, J. Meneses Alonso, P. Flores, C. Castejon, Enhanced modelling of planar radial-loaded deep groove ball bearings with smooth-contact formulation, Multibody Syst. Dyn. 60 (2024) 121–159, https://doi.org/10.1007/s11044-023-09952-2.
[10] O. Halminen, J.F. Aceituno, J.L. Escalona, J. Sopanen, A. Mikkola, Models for dynamic analysis of backup ball bearings of an AMB-system, Mech. Syst. Signal Process. 95 (2017) 324–344, https://doi.org/10.1016/j.ymssp.2017.03.033.
[11] Y. Liu, Z. Zhang, Skidding research of a high-speed cylindrical roller bearing with beveled cage pockets, Ind. Lubr. Tribol. 72 (2020) 969–976, https://doi.org/10.1108/ILT-10-2019-0414.
[12] C. Fang, X. Hu, Q. Chang, W. Zhou, X. Liu, Fault dynamic modeling for cylindrical roller bearings considering cage fracture and raceway defects, Eng. Fail. Anal. 169 (2025) 109152, https://doi.org/10.1016/j.engfailanal.2024.109152.
[13] H. Xu, H. Ren, D. Qin, Dynamic characteristics of the planetary gear system with rolling bearing, Multibody Syst. Dyn. 59 (2023) 171–191, https://doi.org/10.1007/s11044-023-09905-9.
[14] J. Liu, X. Li, M. Xia, A dynamic model for the planetary bearings in a double planetary gear set, Mech. Syst. Signal Process. 194 (2023) 110257, https://doi.org/10.1016/j.ymssp.2023.110257.
[15] J. Liu, Y. Shao, Overview of dynamic modelling and analysis of rolling element bearings with localized and distributed faults, Nonlinear Dyn. 93 (2018) 1765–1798, https://doi.org/10.1007/s11071-018-4314-y.
[16] S.G. Kumbhar, E. Sudhagar P, R.G. Desavale, An overview of dynamic modeling of rolling-element bearings, Noise Vib. Worldw. 52 (2021) 3–18, https://doi.org/10.1177/0957456520948279.
[17] P.K. Gupta, Advanced Dynamics of Rolling Elements, Springer, New York, USA, 1984.
[18] P.K. Gupta, Current status of and future innovations in rolling bearing modeling, Tribol. Trans. 54 (2011) 394–403, https://doi.org/10.1080/10402004.2010.551805.
[19] P.K. Gupta, Transient ball motion and skid in ball bearings, J. Lubr. Technol. 97 (1975) 261–269, https://doi.org/10.1115/1.3452568.
[20] P.K. Gupta, Generalized dynamic simulation of skid in ball bearings, J. Aircr. 12 (1975) 260–265, https://doi.org/10.2514/3.44442.
[21] P.K. Gupta, E.V. Zaretsky, New stress-based fatigue life models for ball and roller bearings, Tribol. Trans. 61 (2018) 304–324, https://doi.org/10.1080/10402004.2017.1319524.
[22] Y. Jiang, W. Huang, W. Wang, G. Peng, A complete dynamics model of defective bearings considering the three-dimensional defect area and the spherical cage pocket, Mech. Syst. Signal Process. 185 (2023) 109743, https://doi.org/10.1016/j.ymssp.2022.109743.
[23] J. Tian, C. Zhang, H. Liang, D. Guo, Simulation of the load reduction process of high-speed angular contact ball bearing with coupling model of dynamics and thermo-elastohydrodynamic lubrication, Tribol. Int. 165 (2022) 107292, https://doi.org/10.1016/j.triboint.2021.107292.
[24] R. Teutsch, B. Sauer, An alternative slicing technique to consider pressure concentrations in Non-Hertzian line contacts, J. Tribol. 126 (2004) 436–442, https://doi.org/10.1115/1.1739244.
[25] R. Teutsch, Kontaktmodelle und strategien zur simulation von wälzlagern und wälzführungen, Ph.D. Thesis, Kaiserslautern, Germany, 2005.
[26] V. Aul, Kontaktmodelle zur dynamischen simulation vollrolliger Zylinderrollenlager, Ph.D. Thesis, Kaiserslautern, Germany, 2014.
[27] P. Wingertszahn, S. Graf, O. Koch, Dynamikmodelle verschiedener wälzlagertypen: betriebsverhalten von kegelrollenlagern in abhängigkeit der belastungssituation im antriebssystem. Abschlussbericht Zum Forschungsvorhaben Nr. 625 III (Heft 1598), Forschungsvereinigung Antriebstechnik e.V., Frankfurt am Main, Germany, 2024.
[28] P. Wingertszahn, O. Koch, L. Maccioni, F. Concli, B. Sauer, Predicting friction of tapered roller bearings with detailed multi-body simulation models, Lubricants 11 (2023) 369, https://doi.org/10.3390/lubricants11090369.
[29] T. Sakaguchi, K. Harada, Dynamic analysis of cage behavior in a tapered roller bearing, J. Tribol. 128 (2006) 604–611, https://doi.org/10.1115/1.2197527.
[30] T. Sakaguchi, K. Harada, Dynamic analysis of cage stress in tapered roller bearings using component-mode-synthesis method, J. Tribol. 131 (2009) 011102, https://doi.org/10.1115/1.3002326.
[31] D. Fritzson, J. Ståhl, G. Morales-Espejel, Simulation of fretting fatigue in conformal and concentrated contacts, Tribol. Online 6 (2011) 64–70, https://doi.org/10.2474/trol.6.64.
[32] I. Nakhimovski, Contributions to the modeling and simulation of mechanical systems with detailed contact analyses, Ph.D. Thesis, Linköping, Sweden, 2006.
[33] L.-E. Stacke, D. Fritzson, Dynamic behaviour of rolling bearings: simulations and experiments, Proc. Inst. Mech. Eng. J. J. Eng. Tribol. 215 (2001) 499–508, https://doi.org/10.1243/1350650011543754.
[34] L.-E. Stacke, D. Fritzson, P. Nordling, BEAST—a rolling bearing simulation tool, Proc. Inst. Mech. Eng. K J. Multi-Body Dyn. 213 (1999) 63–71, https://doi.org/10.1243/1464419991544063.
[35] E. Ioannides, L.-E. Stacke, D. Fritzson, I. Nakhimovski, Multibody rolling bearing calculations: computer program BEAST, in: Proceedings of the World Tribology Congress III, Washington, D.C., USA, ASME, New York, USA, 2005, pp. 903–904.
[36] H. Aramaki, Y. Nakano, Y. Shoda, Rolling bearing analysis codes "BRAIN" - the estimation of rolling bearing performance for an automotive application, SAE Tech. Pap. (1997), https://doi.org/10.4271/970586.
[37] H. Aramaki, Rolling bearing analysis program package "BRAIN", Motion Control 3 (1997) 15–24.
[38] L. Houpert, CAGEDYN: a contribution to roller bearing dynamic calculations part I: basic tribology concepts, Tribol. Trans. 53 (2009) 1–9, https://doi.org/10.1080/10402000903132093.
[39] L. Houpert, CAGEDYN: a contribution to roller bearing dynamic calculations. Part III: experimental validation, Tribol. Trans. 53 (2010) 848–859, https://doi.org/10.1080/10402004.2010.496069.

[40] L. Houpert, CAGEDYN: a contribution to roller bearing dynamic calculations part II: description of the numerical tool and its outputs, Tribol. Trans. 53 (2009) 10–21, https://doi.org/10.1080/10402000903132101.
[41] R.D. Evans, L. Houpert, F. Scandella, M.G. Wilmer, T. Klaehn, A.D. Buchanan, Dynamic analysis of rail gearbox bearings, Proc. Inst. Mech. Eng. F J. Rail Rapid Transit. 231 (2017) 991–996, https://doi.org/10.1177/0954409716656219.
[42] D. Vlasenko, B. Hahn, Modeling of Elastic Cages in the Rolling Bearing Multi-Body Tool CABA3D, in: Multibody Dynamics 2019, Duisburg, Germany, Springer, Cham, Switzerland, 2020, pp. 96–103.
[43] V. Vesselinov, Dreidimensionale simulation der dynamik von Wälzlagern, Ph.D. Thesis, Karlsruhe, Germany, 2003.
[44] S. Schwarz, H. Grillenberger, O. Graf-Goller, M. Bartz, S. Tremmel, S. Wartzack, Using machine learning methods for predicting cage performance criteria in an angular contact ball bearing, Lubricants 10 (2022) 25, https://doi.org/10.3390/lubricants10020025.
[45] K. Heider, Berücksichtigung der schmierstoffhydrodynamik und der käfigverformung in der wälzlagerdynamiksimulation unter hohen zentripetalbeschleunigungen, Ph.D. Thesis, Erlangen-Nürnberg, Germany, 2019.
[46] N. Ghaisas, C.R. Wassgren, F. Sadeghi, Cage instabilities in cylindrical roller bearings, J. Tribol. 126 (2004) 681–689, https://doi.org/10.1115/1.1792674.
[47] M. Wolf, A. Sanner, A. Fatemi, A semi-analytical approach for rapid detection of roller-flange contacts in roller element bearings, Proc. Inst. Mech. Eng. J. J. Eng. Tribol. 235 (2021) 1440–1449, https://doi.org/10.1177/1350650120964295.
[48] M. Bao, L. Wang, K. Niu, D. Zheng, C. Zhang, Dynamic behavior analysis of cylindrical roller bearings with trilobe outer raceway: effect of the out-of-roundness, phase angle and initial clearance, Tribol. Int. (2025) 110498, https://doi.org/10.1016/j.triboint.2024.110498.
[49] Y. Xing, Y. Zhang, Y. Zhang, D. Qiao, Y. Pei, Y. Xiao, Dynamic service mechanism of double-row spherical roller bearings due to self-aligning behavior, Machines 11 (2023) 400, https://doi.org/10.3390/machines11030400.
[50] G. Kogan, R. Klein, A. Kushnirsky, J. Bortman, Toward a 3D dynamic model of a faulty duplex ball bearing, Mech. Syst. Signal Process. 54-55 (2015) 243–258, https://doi.org/10.1016/j.ymssp.2014.07.020.
[51] Y. Wang, W. Wang, S. Zhang, Z. Zhao, Investigation of skidding in angular contact ball bearings under high speed, Tribol. Int. 92 (2015) 404–417, https://doi.org/10.1016/j.triboint.2015.07.021.
[52] T. Yao, L. Wang, X. Liu, Y. Huang, Multibody dynamics simulation of thin-walled four-point contact ball bearing with interactions of balls, ring raceways and crown-type cage, Multibody Syst. Dyn. 48 (2020) 337–372, https://doi.org/10.1007/s11044-019-09704-1.
[53] M. Vehviläinen, P. Rahkola, J. Keränen, J. Halme, J. Sopanen, O. Liukkonen, A. Holopainen, K. Tammi, A. Belahcen, Adapting geometry-based polygonal contacts for simulating faulty rolling bearing dynamics, Mech. Mach. Theory 192 (2024) 105552, https://doi.org/10.1016/j.mechmachtheory.2023.105552.
[54] J. Sopanen, A. Mikkola, Dynamic model of a deep-groove ball bearing including localized and distributed defects. Part 1: theory, Proc. Inst. Mech. Eng. K J. Multi-Body Dyn. 217 (2003) 201–211, https://doi.org/10.1243/14644190360713551.
[55] J. Sopanen, A. Mikkola, Dynamic model of a deep-groove ball bearing including localized and distributed defects. Part 2: implementation and results, Proc Inst. Mech. Eng. K J. Multi-Body Dyn. 217 (2003) 213–223, https://doi.org/10.1243/14644190360713560.
[56] V. Saheta, Dynamics of rolling element bearings using discrete element method, Master Thesis, West Lafayette, USA, 2001.
[57] Y. Liu, Z. Chen, L. Tang, W. Zhai, Skidding dynamic performance of rolling bearing with cage flexibility under accelerating conditions, Mech. Syst. Signal Process. 150 (2021) 107257, https://doi.org/10.1016/j.ymssp.2020.107257.
[58] D. Zhao, J. Hong, K. Yan, Q. Zhao, B. Fang, Dynamic interaction between the rolling element and cage of rolling bearing considering cage flexibility and clearance, Mech. Mach. Theory 174 (2022) 104905, https://doi.org/10.1016/j.mechmachtheory.2022.104905.
[59] R. Dahiwal, Contribution to the influence of cage wear on the bearing life of solid-lubricated rolling bearings, Ph.D. Thesis, Kaiserslautern, Germany, 2021.
[60] T. Yao, Y. Chi, Y. Huang, Research on flexibility of bearing rings for multibody contact dynamics of rolling bearings, Procedia Eng. 31 (2012) 586–594, https://doi.org/10.1016/j.proeng.2012.01.1071.
[61] N. Weinzapfel, F. Sadeghi, A discrete element approach for modeling cage flexibility in ball bearing dynamics simulations, J. Tribol. 131 (2009), https://doi.org/10.1115/1.3063817.
[62] S. Ma, C. Tian, C. Yang, K. Yan, L. Stefano, J. Hong, New bearing model with flexible cage and study of dynamic behavior under variable-speed, Mech. Syst. Signal Process. 208 (2024) 111045, https://doi.org/10.1016/j.ymssp.2023.111045.
[63] H. Li, H. Li, Y. Liu, H. Liu, Dynamic characteristics of ball bearing with flexible cage lintel and wear, Eng. Fail. Anal. 117 (2020) 104956, https://doi.org/10.1016/j.engfailanal.2020.104956.
[64] A. Ashtekar, F. Sadeghi, A new approach for including cage flexibility in dynamic bearing models by using combined explicit finite and discrete element methods, J. Tribol. 134 (2012) 041502, https://doi.org/10.1115/1.4007348.
[65] W. LaCava, Y. Xing, C. Marks, Y. Guo, T. Moan, Three-dimensional bearing load share behaviour in the planetary stage of a wind turbine gearbox, IET Renew. Power Gener. 7 (2013) 359–369, https://doi.org/10.1049/iet-rpg.2012.0274.
[66] Z. Jiang, Y. Xing, Y. Guo, T. Moan, Z. Gao, Long-term contact fatigue analysis of a planetary bearing in a land-based wind turbine drivetrain, Wind Energy 18 (2015) 591–611, https://doi.org/10.1002/we.1713.
[67] J. Tan, C. Zhu, C. Song, Y. Li, X. Xu, Dynamic modeling and analysis of wind turbine drivetrain considering platform motion, Mech. Mach. Theory 140 (2019) 781–808, https://doi.org/10.1016/j.mechmachtheory.2019.06.026.
[68] Y. Xu, J. Liu, X. Li, C. Tang, An investigation of vibrations of a flexible rotor system with the unbalanced force and time-varying bearing force, Chin. J. Mech. Eng. 38 (2025), https://doi.org/10.1186/s10033-025-01186-x.
[69] M.D. Brouwer, F. Sadeghi, A. Ashtekar, J. Archer, C. Lancaster, Combined explicit finite and discrete element methods for rotor bearing dynamic modeling, Tribol. Trans. 58 (2015) 300–315, https://doi.org/10.1080/10402004.2014.968699.
[70] L. Cao, M.D. Brouwer, F. Sadeghi, L.-E. Stacke, Effect of housing support on bearing dynamics, J. Tribol. 138 (2016) 011105, https://doi.org/10.1115/1.4031104.
[71] A. Shafiee, F. Sadeghi, M.G. Wilmer, An integrated finite element and adams modeling approach for analyzing rotor-bearing housing systems, J. Tribol. 147 (2025) 014303, https://doi.org/10.1115/1.4066205.
[72] R.R. Craig, M.C.C. Bampton, Coupling of substructures for dynamic analyses, AIAA J. 6 (1968) 1313–1319, https://doi.org/10.2514/3.4741.
[73] Y. Li, H. Cao, L. Niu, X. Jin, A general method for the dynamic modeling of ball bearing–Rotor systems, J. Manuf. Sci. Eng. 137 (2015) 021016, https://doi.org/10.1115/1.4029312.
[74] J. Tian, C. Zhang, Z. Wang, H. Su, D. Wang, D. Guo, Radial load analysis of matched angular contact ball bearings in bearing-rotor system, Mech. Syst. Signal Process. 211 (2024) 111188, https://doi.org/10.1016/j.ymssp.2024.111188.
[75] D. He, Y. Yang, H. Xu, H. Ma, X. Zhao, Dynamic analysis of rolling bearings with roller spalling defects based on explicit finite element method and experiment, J. Nonlinear Math. Phys. 29 (2022) 219–243, https://doi.org/10.1007/s44198-022-00027-y.
[76] J. Liu, Y. Xu, Y. Shao, H. Xiao, H. Li, The effect of a localized fault in the planet bearing on vibrations of a planetary gear set, J. Strain Anal. Eng. Des. 53 (2018) 313–323, https://doi.org/10.1177/0309324718769491.
[77] C. Wagner, A. Krinner, T. Thümmel, D. Rixen, Full dynamic ball bearing model with elastic outer ring for high speed applications, Lubricants 5 (2017) 17, https://doi.org/10.3390/lubricants5020017.
[78] S. Leupold, R. Schelenz, G. Jacobs, Method to determine the local load cycles of a blade bearing using flexible multi-body simulation, Forsch Ingenieurwes 85 (2021) 211–218, https://doi.org/10.1007/s10010-021-00457-y.
[79] J. Fiszer, T. Tamarozzi, W. Desmet, A semi-analytic strategy for the system-level modelling of flexibly supported ball bearings, Meccanica 51 (2016) 1503–1532, https://doi.org/10.1007/s11012-015-0318-6.
[80] C. Defaye, D. Nelias, A. Leblanc, F. Bon, Theoretical analysis of high-speed cylindrical roller bearing with flexible rings mounted in a squeeze film damper, Tribol. Trans. 51 (2008) 762–770, https://doi.org/10.1080/10402000801911804.
[81] A. Leblanc, D. Nelias, C. Defaye, Nonlinear dynamic analysis of cylindrical roller bearing with flexible rings, J. Sound Vib. 325 (2009) 145–160, https://doi.org/10.1016/j.jsv.2009.03.013.

[82] J. Liu, C. Tang, Y. Shao, An innovative dynamic model for vibration analysis of a flexible roller bearing, Mech. Mach. Theory 135 (2019) 27–39, https://doi.org/10.1016/j.mechmachtheory.2019.01.027.
[83] R. Dahiwal, A. Aschenbrenner, B. Schleich, S. Wiesker, T. Kiekbusch, S. Tremmel, S. Wartzack, Evaluation of the effects of geometrical deviations on the fatigue life and vibrations of cylindrical roller bearings, Bear World J. 3 (2018) 7–21.
[84] J.A. Wensing, Ph.D. Thesis, Twente, Netherlands, 1998.
[85] S. Kerst, B. Shyrokau, E. Holweg, A semi-analytical bearing model considering outer race flexibility for model based bearing load monitoring, Mech. Syst. Signal Process. 104 (2018) 384–397, https://doi.org/10.1016/j.ymssp.2017.11.008.
[86] M. Raabe, Consideration of elastic deformations of gear bodies using a reduction on a Fourier series, Forsch Ingenieurwes 83 (2019) 461–468, https://doi.org/10.1007/s10010-019-00362-5.
[87] A.A. Shabana, Dynamics of Multibody Systems, 5th ed., Cambridge University Press, Cambridge, England, 2020.
[88] ISO 16281: Rolling bearings - methods for calculation the modified reference rating life for universally loaded bearings, 2025.
[89] Bearinx, High-Level Bearing Design, Schaeffler Technologies AG & Co. KG, Herzogenaurach, Germany, 2021.
[90] R.J. Guyan, Reduction of stiffness and mass matrices, AIAA J. 3 (1965) 380, https://doi.org/10.2514/3.2874.
[91] V. Makhavikou, Line-fitting method of model order reduction for elastic multibody systems, Ph.D. Thesis, Magdeburg, Germany, 2015.
[92] D. Yang, X. Wang, Y. Hou, An improved slicing technique for finite line contacts in the modeling of rolling element bearings, J. Tribol. 145 (2023) 084302, https://doi.org/10.1115/1.4062364.
[93] G. Lundberg, Elastische berührung zweier halbräume, Forsch Ingenieurwes 10 (1939) 201–211, https://doi.org/10.1007/BF02584950.
[94] A. Sjö, Numerical aspects in contact mechanics and rolling bearing simulation, Ph.D. Thesis, Lund, Sweden, 1996.
[95] S. Wirsching, M. Marian, M. Bartz, T. Stahl, S. Wartzack, Geometrical optimization of the EHL roller face/rib contact for energy efficiency in tapered roller bearings, Lubricants 9 (2021) 67, https://doi.org/10.3390/lubricants9070067.
[96] P. Dietl, Damping and stiffness characteristics of rolling element bearings: theory and experiment, Ph.D. Thesis, Wien, Austria, 1997.
[97] O. Koch, J. Binderszewsky, C. Bohnert, B. Hahn, D. Witt, Dynamic rolling bearing simulation: usage as virtual bearing test rig, in: antriebstechnisches Kolloquium ATK 2013, Aachen, Germany, Apprimus, Aachen, Germany, 2013, pp. 155–170.
[98] O. Koch, R. Plank, J. Weber, Bearing optimization due to three-dimensional dynamic simulation. Gleit- und Wälzlagerungen, Wiesloch, Germany, VDI Verlag, Düsseldorf, Germany, 2009, pp. 43–51.
[99] M. Krimpmann, V. Vesslinov, J. Weber, Numerische und experimentelle analyse der kinematik von Rollenlagern. Gleit- und Wälzlagerungen, Fulda, Germany, VDI Verlag, Düsseldorf, Germany, 2002, pp. 377–398.
[100] J. Burkardt, SLATEC: a mathematical library. https://people.math.sc.edu/Burkardt/f_src/slatec/slatec.html.
[101] MESYS Rolling Bearing Calculation, MESYS Calculation Software User Manual. Version 06/2024, MESYS AG, Zürich, Switzerland, 2025.
[102] D. Quitzrau, S. Lenssen, H. Golbach, Bearing design with Bearinx: calculation in the complete elastic system, in: antriebstechnisches Kolloquium ATK 2013, Aachen, Germany, Apprimus, Aachen, Germany, 2013, pp. 171–192.
[103] T.A. Harris, M.N. Kotzalas, Essential Concepts of Bearing Technology, 5th ed., CRC Press, Boca Raton, USA, 2006.
[104] Y. Hou, X. Wang, Measurement of load distribution in a cylindrical roller bearing with an instrumented housing: finite element validation and experimental study, Tribol. Int. 155 (2021) 106785, https://doi.org/10.1016/j.triboint.2020.106785.
[105] T. Russell, A. Shafiee, B. Conley, F. Sadeghi, Evaluating load distribution at the bearing-housing interface using thin film pressure sensors, Tribol. Int. 165 (2022) 107293, https://doi.org/10.1016/j.triboint.2021.107293.
[106] Z.-Q. Qu, Model Order Reduction Techniques: With Applications in Finite Element Analysis, Springer London, London, England, 2004.
[107] J. Liu, L. Wang, Z. Shi, Dynamic modelling of the defect extension and appearance in a cylindrical roller bearing, Mech. Syst. Signal Process. 173 (2022) 109040, https://doi.org/10.1016/j.ymssp.2022.109040.
[108] M. Nakhaeinejad, M.D. Bryant, Dynamic modeling of rolling element bearings with surface contact defects using bond graphs, J. Tribol. 133 (2011) 011102, https://doi.org/10.1115/1.4003088.
[109] R. Zhang, L. Guo, Z. Zong, H. Gao, M. Qian, Z. Chen, Dynamic modeling and analysis of rolling bearings with rolling element defect considering time-varying impact force, J. Sound Vib. 562 (2023) 117820, https://doi.org/10.1016/j.jsv.2023.117820.